Monthly Notices of the ROYAL ASTRONOMICAL SOCIETY

MNRAS **518,** 5500–5521 (2023) https://doi.org/10.1093/mnras/stac3448
Advance Access publication 2022 November 25

MASCOT: molecular gas depletion times and metallicity gradients – evidence for feedback in quenching active galaxies

C. Bertemes [1]★ D. Wylezalek [1] M. Albán,[1] M. Aravena,[2] W. M. Baker [3,4] S. Cazzoli [5] C. Cicone,[6] S. Martín [7,8] A. Schimek,[6] J. Wagg[9] and W. Wang [1]

[1]*Zentrum für Astronomie der Universität Heidelberg, Astronomisches Rechen-Institut Mönchhofstr, 12-14 D-69120 Heidelberg, Germany*
[2]*Núcleo de Astronomía, Facultad de Ingeniería y Ciencias, Universidad Diego Portales, Av. Ejército 441, Santiago, Chile*
[3]*Kavli Institute for Cosmology, University of Cambridge, Madingley Road, Cambridge CB3 OHA, UK*
[4]*Cavendish Laboratory - Astrophysics Group, University of Cambridge, 19 JJ Thompson Avenue, Cambridge CB3 OHE, UK*
[5]*IAA - Instituto de Astrofísica de Andalucía (CSIC), Apdo. 3004, E-18008 Granada, Spain*
[6]*Institute of Theoretical Astrophysics, University of Oslo, PO Box 1029, Blindern 0315, Oslo, Norway*
[7]*European Southern Observatory, Alonso de Córdova, 3107, Vitacura, Santiago, 763-0355, Chile*
[8]*Joint ALMA Observatory, Alonso de Córdova, 3107, Vitacura, Santiago, 763-0355, Chile*
[9]*SKA Observatory, Lower Withington Macclesfield, Cheshire SK11 9FT, UK*

Accepted 2022 November 19. Received 2022 November 14; in original form 2022 August 8

ABSTRACT

We present results from the first public data release of the MaNGA-ARO Survey of CO Targets (MASCOT), focusing our study on galaxies whose star formation rates and stellar masses place them below the ridge of the star-forming main sequence. In optically selected type 2 AGN/low-ionization nuclear emission regions (LINERs)/Composites, we find an empirical relation between gas-phase metallicity gradients ∇Z and global molecular gas depletion times $t_{\rm dep} = M_{\rm H_2}/{\rm SFR}$ with 'more quenched' systems showing flatter/positive gradients. Our results are based on the O3N2 metallicity diagnostic (applied to star-forming regions within a given galaxy), which was recently suggested to also be robust against emission by diffuse ionized gas (DIG) and LINERs. We conduct a systematic investigation into possible drivers of the observed $\nabla Z - t_{\rm dep}$ relation (ouflows, gas accretion, *in situ* star formation, mergers, and morphology). We find a strong relation between ∇Z or $t_{\rm dep}$ and centralized outflow strength traced by the [O III] velocity broadening. We also find signatures of suppressed star formation in the outskirts in AGN-like galaxies with long depletion times and an enhancement of metals in the outer regions. We find no evidence of inflows impacting the metallicity gradients, and none of our results are found to be significantly affected by merger activity or morphology. We thus conclude that the observed ∇Z–$t_{\rm dep}$ relation may stem from a combination of metal redistribution via weak feedback, and a connection to *in situ* star formation via a resolved mass-metallicity–SFR relation.

Key words: galaxies: active – galaxies: evolution – galaxies: ISM – galaxies: kinematics and dynamics.

1 INTRODUCTION

One of the key goals in galaxy evolution is to quantify the growth of galaxies, which occurs via the conversion of gas into stars. Specifically, the fuel for star formation is held in the form of a cold, molecular gas phase, which fragments and contracts via cooling until a critical density is reached and gravitational collapse ensues, culminating in the ignition of nuclear fusion and thus the birth of new stars (e.g. Schmidt 1959; Kennicutt 1998). During the actively star-forming phase in the lives of galaxies, their growth is further characterized by an observed tight relation between their star formation rate (SFR) and the stellar mass $M_\star$ already in place. This relation is known as the main sequence (MS) of star-forming galaxies (e.g. Brinchmann et al. 2004; Noeske et al. 2007; Renzini & Peng 2015). It has been suggested to arise as a combination of the Kennicutt–Schmidt relation between molecular gas mass surface density and SFR surface density (Schmidt 1959; Kennicutt 1998), and the 'molecular gas MS' between between the stellar and molecular gas mass surface densities (Lin et al. 2019; Baker et al. 2022b). The star-forming branch around the MS can be contrasted to the locus of passive galaxies, and their ensemble forms a bimodal distribution in the SFR–$M_\star$ plane. The regime in between both populations, dubbed the Green Valley, is sparsely populated, which has been suggested to point to rapid quenching as galaxies transition from the star forming into the passive regime towards the end of their life (see Salim 2014 for a review).

Studies of the cold neutral gas phase hold important clues for characterizing and understanding SFR fluctuations and the quenching of galaxies, and thus represent a prime element in compiling a theory of galaxy evolution. For instance, it has been shown that galaxies below the MS do not only have a lower quantity of molecular gas, but are also less efficient at converting their remaining gas into stars (e.g. Saintonge et al. 2017; see also Saintonge & Catinella 2022 for a detailed review). The recent rise of state-of-the-art integral field unit (IFU) and multi-object spectroscopy (MOS) facilities enables studies to go beyond investigating how molecular gas properties shape galaxies in a global way by resolving galaxies as extended dynamic sys-

★ E-mail: c.bertemes@uni-heidelberg.de

tems. For instance, the Extragalactic Database for Galaxy Evolution – Calar Alto Integral Field Area survey (EDGE-CALIFA; Bolatto et al. 2017) and Atacama Large Millimeter Array (ALMA)-MaNGA QUEnching and STar formation surveys (ALMaQUEST; Lin et al. 2020) have conducted resolved CO emission line radio observations on samples of galaxies with optical-IFU data. The EDGE-CALIFA collaboration performed CO follow-up observations of 177 galaxies with existing CALIFA data with the Combined Array for Millimeter-wave Astronomy interferometer, which will further be expanded by ongoing observations with the APEX telescope (295 targets to date; Colombo et al. 2020). The goal of this survey is to study the resolved relationships between molecular gas and e.g. stellar mass and SFR, ionized gas kinematics, dust extinction, and physical and chemical conditions within galaxies. For instance, Colombo et al. (2020) found evidence for a scenario in which the quenching of galaxies starts with an initial central shortage of molecular gas, but then in a second phase a decrease in star-forming efficiency becomes the most important driver for permanently pushing galaxies into quiescence. Within the ALMaQUEST survey (described in more detail in Section 2.2), starbursts selected to feature at least a 50 per cent elevation of the SFR in the central region were shown to be primarily driven by an increased star-forming efficiency (Ellison et al. 2020), which is the ratio of the SFR over the molecular gas mass $M_{\rm H_2}$. On the other hand, Green Valley galaxies show both suppressed star-forming efficiencies and molecular gas fractions ($M_{\rm H_2}/M_\star$) with respect to the MS, both in star forming as well as 'retired' spaxels (Lin et al. 2022). We also refer the reader to Sánchez et al. (2021a, 2021b) for a summary of the resolved and integrated relations between molecular gas mass, SFR and stellar mass, and the connection between the different scales.

Complementing the ALMaQUEST and EDGE-CALIFA survey, Wylezalek et al. (2022) recently published the first data release of our Mapping Nearby Galaxies at Apache Point Observatory-Arizona Radio Observatory (MaNGA-ARO) Survey of CO Targets (MASCOT). Using 12m single-dish ^{12}CO(1-0) observations with the ARO, we have collected data for 187 galaxies from the MaNGA survey (Bundy et al. 2015) to date, selected to span a broad range in stellar masses ($\sim$1.5 dex) and sSFR = SFR/M$_\star$ (>3 dex). Our observations thus enhance the number statistics of galaxies with simultaneously available optical-IFU data and (galaxy-integrated) CO observations. Further observations are still ongoing. We note that MASCOT is highly complementary to ALMaQUEST in terms of the field of view probed by the CO observations (while drawing from the identical underlying optical-IFU survey), and therefore we include the public global ALMaQUEST data in Wylezalek et al. (2022) together with the MASCOT DR1 for convenience.

In this paper, we present results based on the first data release. In particular, we combine the study of molecular gas properties with resolved metallicities and kinematics, as the latter are, amongst others, sensitive to gas accretion, feedback mechanisms, and *in situ* star formation. We also investigate to what extent inflows/outflows have any measurable impact on star formation via influencing the availability of fuel, or its consumption.

In recent years, resolved chemical abundance studies have brought to light the diversity of gas-phase metallicity gradients present within galaxies, reflecting the variety of physical processes that shape them. The majority of galaxies in the nearby Universe are found to exhibit negative gas-phase metallicity gradients, i.e. they are more metal-rich in their central regions than in the outskirts (see e.g. Sánchez et al. 2014 and the review by Maiolino & Mannucci 2019). This is qualitatively consistent with an inside-out growth scenario in which stellar populations in the centre have more time to chemically pollute their surroundings. Further, Belfiore et al. (2017) and Poetrodjojo et al. (2018) found evidence for a mass–metallicity gradient relation complementing the established mass–tallicity relation. The latter has been suggested to emerge from a relation on resolved scales between local metallicities and stellar mass surface densities tracing morphology (Barrera-Ballesteros et al. 2016; Lutz et al. 2021). The dependence of the radial metallicity distribution on both mass and morphology has also been shown in Sánchez (2020, 2021a; figs 15 and 16, respectively). Boardman et al. (2021, 2022) further found metallicity gradients to steepen with galaxy size at fixed mass, which they traced back to variations of the local stellar-mass surface density relative to the total stellar mass. Resolved metallicities have also been found to show a weaker dependence on global H I mass fraction (Franchetto et al. 2021) or absolute H I mass (Lutz et al. 2021), which is consistent with a 'local gas regulator model' balancing gas accretion, star formation, and outflows. Using a numerical chemical evolution model, Lian et al. (2018a, b) argue that reproducing both the observed global mass–metallicity relation and metallicity gradients requires including either the impact of chemically enriched outflows or radial variations in the initial mass function. Similarly, Hemler et al. (2021) show that feedback processes by active galactic nuclie (AGNs) and stars in Illustris TNG50 flatten metallicity gradients over time to reproduce the observed population at low redshift, while FIRE simulations predict that bursty star formation and feedback can significantly change metallicity gradients on sub-Gyr time-scales at high redshift (Ma et al. 2017). Baker et al. (2022a) further demonstrate that local metallicities in MaNGA galaxies depend more strongly on the global SFR than on the local one, which may be interpreted in terms of stellar feedback redistributing chemically enriched material.

Studying the connection between the chemical distribution, gas flows, star formation, and molecular gas properties is of particular interest in the regime below the MS, including the Green Valley, to uncover information about the drivers of quenching. However, (resolved) metallicity studies have traditionally been sparse in the below-MS regime given the prevalence of diffuse ionized gas (DIG) contamination. One approach is to limit the analysis to star-forming regions within those galaxies with DIG emission (e.g. Sánchez et al. 2018). Recent works have further investigated to what extent DIG emission, as well as low-ionization (nuclear) emission-line regions (LINERs/LIERs), may or may not bias strong-line metallicity calibrators (Zheng et al. 2017; Kumari et al. 2019; Vale Asari et al. 2019). For the O3N2 metallicity diagnostic (based on Hα, [N III] λ6583, Hβ, and [O III] λ5007) in particular, the bias on recovered metallicity gradients was found to be limited to $\lesssim$0.05 dex and, importantly, symmetric (such that it is unlikely to give rise to artificial correlations in any statistical analysis). Motivated by these findings (summarized in more detail in Section 2.4), we therefore focus on the below/on-MS regime in this work, using the O3N2 diagnostic to study the interplay between metallicity gradients and molecular gas properties, and furthermore include LI(N)ERs and Composites in our analysis. To exercise caution, we will still use metallicity gradients derived via star formation-dominated subfields within a given galaxy.

The paper is organized as follows. In Section 2, we describe the data products we use, including a more detailed description of the MASCOT observations. We also motivate our choice of metallicity diagnostics and present the sample selection. In Section 3, we present the main focus of this paper, namely a relation found between metallicity gradients ∇Z and molecular gas depletion time $t_{\rm dep} = M_{\rm H_2}/{\rm SFR}$ within AGN, LINERs, and Composites below/on the MS, while also performing sanity checks about the robustness of this relation. In Section 4, we expand our data analysis by investigating the viability of several possible drivers behind the

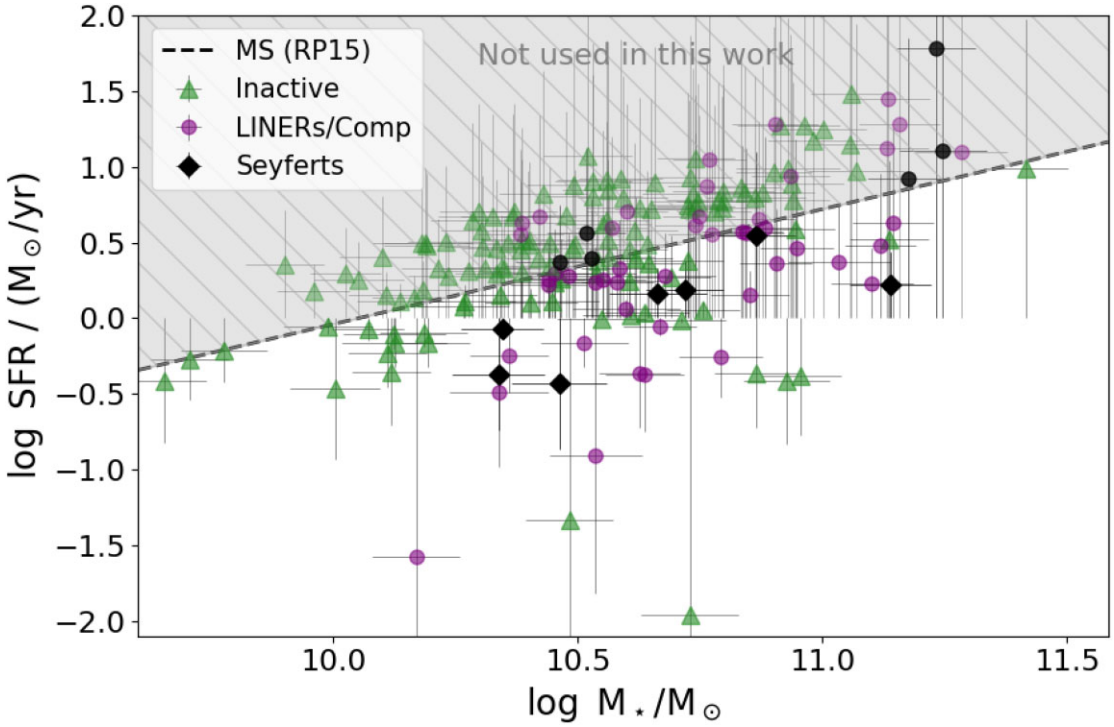

Figure 1. Location of the MASCOT sample within the plane of star formation rate SFR versus stellar mass $M_\star$. The Renzini & Peng (2015) MS relation is shown as a dashed line. In this work, we focus on the below/on-MS regime and thus discard the targets above the MS ridge as illustrated by the grey hatched region. The green data points correspond to inactive galaxies, the purple ones to LINERs and Composites, and the black ones to Seyfert AGN, according to a Baldwin, Phillips & Terlevich (1981) classification based on their central kpc.

∇Z–$t_{\rm dep}$ relation: gas flows, *in situ* star formation, mergers, and morphology. Finally, we proceed to summarize our findings in Section 5. Throughout this paper, we assume a standard cosmology with $H_0 = 70\ {\rm km\,s^{-1}\ Mpc^{-1}}$, $\Omega_m = 0.3$, and $\Omega_\Lambda = 0.7$.

2 DATA AND METHODS

2.1 MASCOT

Our primary data set is the MASCOT (first data release presented in Wylezalek et al. 2022). MASCOT is an ESO Public Spectroscopic Survey using the ARO to conduct single-dish CO(1-0) follow-up observations of galaxies with existing optical-IFU data from the MaNGA survey, which will be summarized below in Section 2.3. The main objective of MASCOT is to investigate the relation between molecular gas properties and spatially resolved optically derived quantities. In particular, the size of the sample (consisting of $\sim$ 20 per cent of AGN/LINERs/Composites) enables us to investigate how such relations vary for galaxies with different levels of star-forming and AGN activity, and examine the role of morphology and environment.

Observations were carried out using the 3mm receiver on the 12m ARO antenna (equivalent to ALMA Band 3, 84–116 GHz). The ARO beam size is $\sim$55 arcsec. To inform our observing strategy, we performed on-the-fly-data reduction and stayed on-target until we either obtained a detection at the level of $\gtrsim 5\sigma$, reached a sensitivity limit of rms = 0.25 mK (using velocity bins of $\sim$ 50km s^{-1}), reached the end of a given observing block, or the telescope required a point-focus. Moreover, we prioritized targets according to their visibility (i.e. low air masses), whilst avoiding pointing the antenna directly into the Sun or the wind. Besides visibility considerations, our sample was further designed to span a broad range in stellar masses with $\log M_\star > 9.5\,{\rm M_\odot}$ and specific SFRs focused around the MS, as well as including a number of Green Valley galaxies and starbursts. In more detail, the first data release consists of 187 galaxies spanning over 1.5 dex in stellar mass and over 3 orders of magnitude in sSFR. Fig. 1 shows the position of our targets in the MS plane, supplemented by the ALMaQUEST survey (see Section 2.2 below). The dashed line shows the local MS relation obtained by Renzini & Peng (2015). In this work, we exclude all galaxies above the dashed line and select those falling below it to focus on the regime below the MS, as well as on it (given the uncertainties in the data points and the intrinsic scatter around the MS of $\sim$0.3 dex). Our sample contains inactive galaxies, as well as LINERs/Composites and Seyfert AGN, which are coloured in green, purple, and black, respectively, according to a Baldwin et al. (1981) classification within the central 1 kpc (discussed in more detail in Section 2.5).

We provide the binned and unbinned CO profiles, along with other raw data products (e.g. CO fluxes and luminosities) and derived quantities (e.g. H_2 masses and kinematics of the fitted CO lines), on the MASCOT website.[1] The H_2 masses are derived using the CO-to-H_2 conversion factor $\alpha_{\rm CO}$ from Accurso et al. (2017), which depends on metallicity, as well as offset in SFR from the star-forming MS relation (which we take from Renzini & Peng 2015). The first data release of MASCOT makes use of the stellar masses and SFRs from the Pipe3D catalog (Sánchez et al. 2016, 2018; described in more detail in Section 2.3.2) to calculate molecular gas fractions and depletion times. While the Accurso et al. (2017) $\alpha_{\rm CO}$ conversion was established based on the Pettini & Pagel (2004) calibrator,

[1] https://wwwstaff.ari.uni-heidelberg.de/dwylezalek/mascot.html

metallicities based upon it are not included in the Pipe3D catalog. Wylezalek et al. (2022) therefore uses the Pipe3D oxygen abundances based on the Maiolino et al. (2008) prescription, and corrects for a constant offset of 0.05 with respect to Pettini & Pagel (2004) metallicities within our mass range (Sánchez et al. 2017). In this work, we derive H_2 masses in two ways: first, following Wylezalek et al. (2022) with the metallicity-dependent CO-to-H_2 conversion outlined above, and second, using a constant α_{CO} factor instead.

2.2 ALMaQUEST

We are supplementing our ARO CO(1-0) observations with data from the ALMaQUEST survey (Lin et al. 2020). The ALMaQUEST project used the ALMA to perform spatially resolved CO(1-0) follow-up observations of 46 galaxies included in the MaNGA survey (described in Section 2.3) on kpc scales. Their targets were selected to span a broad range of star-forming activity ranging from starbursts down to CO-fainter Green Valley galaxies. The field of view at the CO(1-0) frequency is ∼50 arcsec, broadly similar to the ARO beam size of ∼55 arcsec from our MASCOT observations. Galaxy-integrated measurements from ALMaQUEST are included in Wylezalek et al. (2022) along with the first MASCOT data release.

2.3 MaNGA

As mentioned above, a primary science goal of the MASCOT survey (Section 2.1) is to study the connection between resolved optically derived galaxy parameters and molecular gas properties via CO(1-0) observations. The required optical-IFU data are taken from the public MaNGA survey, which constitutes the underlying population from which the MASCOT sample is drawn. We now proceed to describe the MaNGA survey and relevant data products in more detail.

2.3.1 MaNGA survey overview

The MaNGA survey (Bundy et al. 2015) is part of the fourth generation of the Sloan Digital Sky Survey (SDSS; Blanton et al. 2017). Launched in 2014 July, MaNGA has been collecting optical-IFU spectra for ∼10k galaxies at low redshift ($\langle z \rangle \sim 0.03$) using the two Baryonic Oscillation Spectroscopic Survey (BOSS) spectrographs mounted on the 2.5 metre Sloan telescope at the Apache Point Observatory. The red and blue arm of the BOSS spectrographs cover the wavelength range from 3600 to 10 300 Å (Smee et al. 2013), with a median spectral resolution $\langle R \rangle \sim 2000$. The MaNGA sample is designed to follow a roughly flat distribution in $\log M_\star$ above 9 $M_\odot$ (Wake et al. 2017), with about two thirds of the targets being observed out to 1.5 R_e ('primary' sample) and the rest being covered out to 2.5 R_e ('secondary' sample). We refer the reader to Law et al. (2015) and Yan et al. (2016a, b) for details on the observational strategy and Data Reduction Pipeline (DRP). The final DRP data cube products are interpolated on a grid of 0.5 × 0.5 arcsec^2 spaxels, corresponding to roughly 1–2 kpc (while the effective angular resolution amounts to ∼2.5 arcsec). All of the MASCOT targets are included in SDSS-IV DR15, and thus we use version 2.4.3 of the MaNGA data products.

2.3.2 Stellar masses, SFRs, and metallicity (gradients) from Pipe3D

In this work, we make use of version 2.4.3 of the public Pipe3D Value Added Catalog (Sánchez et al. 2016, 2018). This data set contains estimates of key galaxy properties, including stellar population properties, star formation histories, emission line models, and stellar absorption indices, as recovered by running the Pipe3D full spectral fitting pipeline using the spectra of MaNGA galaxies on a spaxel-by-spaxel basis. Pipe3D is an iterative fitting procedure (Lacerda et al. 2022) following a similar process to a Markov chain Monte Carlo (MCMC) inference, which derives the best-fitting stellar velocity and velocity dispersion fields in a first step, then proceeds to constrain the amount of dust attenuation with fixed stellar kinematics in a second iteration. The results from these first two steps are then used to fit the continuum as a linear combination of simple stellar population (SSP) templates (with a Salpeter initial mass function) to recover galaxy quantities, while independently modelling the emission lines with multiple Gaussians. The adopted stellar library combines GRANADA theoretical stellar templates (Martins et al. 2005) with the MILES stellar library (Sánchez-Blázquez et al. 2006; Vazdekis et al. 2010; Falcón-Barroso et al. 2011).

In this work, we use the Pipes3D integrated stellar mass, SFR, as well as metallicities and gradients thereof. For our choice of metallicity calibrator, we maintain consistency with Wylezalek et al. (2022) in which the first MASCOT data release was presented and use the Pipe3D oxygen abundances at $1R_e$ based on the Maiolino et al. (2008) prescription ('oh_re_fit_m08"; M08). As we derive H_2 masses using the metallicity-dependent conversion from Accurso et al. (2017) and as those authors used the O3N2 prescription from Pettini & Pagel (2004), we apply a correction of +0.05 dex to the Pipe3D M08 metallicities to account for the offset. However, for the metallicity *gradients* ∇Z, we follow a slightly different approach. Specifically, we use metallicity gradients derived in two different ways: first, given that we are including in our analysis the locus below the MS where DIG levels are elevated, we choose to use an O3N2-based metallicity prescription since the latter was suggested to be reasonably robust in DIG and LI(N)ER regions (Zheng et al. 2017; Kumari et al. 2019; Vale Asari et al. 2019) with no systematic bias (but a symmetric scatter), as we will discuss in more detail in Section 2.4. We therefore choose to use directly the Pipe3D oxygen abundance gradient based on the O3N2 calibrator from Marino et al. (2013) ('alpha_oh_re_fit_o3n2") evaluated within 0.5–2 R_e (which are based on those regions within galaxies ionized by star formation). Secondly, we also use Pipe3D gradients based on the Tremonti et al. (2004) calibrator inferred from the R23 ratio, as the latter has been shown to be less sensitive to ionization (Kewley, Nicholls & Sutherland 2019; their fig. 9), at least within the metallicity range of our data set. We will rely on the O3N2-based metallicity gradients for the main presentation of our results, and conduct a sanity check based on the R23 diagnostic instead in Section 3.2.

2.3.3 Resolved SFRs and stellar masses recovered by a radially resolved full spectral fitting procedure

We carry out a radially resolved full spectral fitting procedure to incorporate the possible impact of the star formation distribution and resolved stellar masses in our analysis. Our approach follows the stellar population synthesis (SPS) method, in which a given spectrum is fitted as a superposition of the emissions from stellar populations of different ages and metallicities. We run our fitting procedure on radial spectra, obtained by dividing each galaxy into annuli of 0.2 R_e width tracing the elliptical Petrosian apertures, and apply aperture corrections to recover the total g-band flux from the NASA-Sloan Atlas catalog (NSA; Blanton et al. 2011). While we defer a detailed description of our fitting procedure to an upcoming paper (Bertemes & Wuyts 2022), it can be briefly summarized

as follows. We use the Bagpipes code (Carnall et al. 2018) to model the observed emission in galactic annuli via a superposition of stellar populations following a two-component star formation history (SFH) consisting of a lognormal and a decoupled recent burst of constant SFR operating over the past 30 Myr. Each of the two SFH components assumes a single stellar metallicity for all of its stars (which for the recent burst corresponds to the gas-phase metallicity). Bagpipes is based on the 2016 version of the Bruzual & Charlot (2003) models, and assumes a Kroupa & Boily (2002) IMF. We simultaneuously fit the MaNGA spectra and associated NSA photometry in the optical wavelength range of 3700–7400 Å, assuming a Calzetti et al. (2000) extinction law. We further assume a fixed ratio of nebular to stellar attenuation $\eta = 1/0.44$ due to birthcloud dust, as also retrieved by Calzetti et al. (2000). Ionized gas emission lines are modelled self-consistently in Bagpipes with CLOUDY (Ferland et al. 1998). However, we mask the [O II] λ3726, 3729 and [S II] λ6716, 6731 lines, as it was found empirically that they were challenging to reproduce simultaneously with the Balmer lines, [O III] λ5007, and [N III] λ6583, which we prioritize as they hold significant information about the SFR, as well as physical and chemical conditions in the ISM. We attribute this challenge to the relatively simplified CLOUDY photoionization model grid used in terms of assumptions about the birthcloud age, metallicity, and ionization parameter. Further, we introduce more freedom to the H α line fitting via a normalization parameter allowed to vary between 1 and 1.5. The rationale behind this parameter is that at fixed SFR, the H α luminosity predicted by Bagpipes (based on its underlying CLOUDY grid) is known to feature a systematic offset with respect to the values predicted by Kennicutt & Evans (2012) of up to 0.2 dex depending on metallicity and ionization. Moreover, we set a logarithmic prior on the time of peak star formation, which was found to be required for consistency with the cosmic SFR density in the photometric fitting runs in Carnall et al. (2019). Finally, we impose a prior following a student's t-distribution on the jump in SFR between the recent burst and the early SFH, which will favour a smooth transition in the absence of constraining information (Leja et al. 2019).

We find that when running our fitting procedure on our sample defined in Section 2.5 below, our recovered global SFRs agree well with the Pipe3D measurements, with only a minor offset of 0.12 dex and a scatter of 0.19 dex. Similarly, our recovered stellar masses are offset from the Pipe3D reference values by <0.001 dex, with a scatter of ∼0.13 dex. Motivated by this agreement, we will use our SPS fitting procedure to derive resolved stellar masses and SFRs within annuli inside galaxies.

2.4 Choice of metallicity calibrator

In this work, we are are focusing on the interplay between resolved metallicities and molecular gas properties in galaxies that are located *below/on the MS*. Below the MS, metallicity studies have traditionally been sparse due to the ubiquity of DIG regions, and concerns about the latter potentially contaminating common metallicity diagnostics. It has been suggested that DIG emission may bias strong-line diagnostics by contributing to the line fluxes entering the calculation (Zhang et al. 2017).

We first note that the gas-phase metallicity gradients that we take from the Pipe3D catalog are based on regions consistent with being ionized pre-dominantly by star formation (Sánchez et al. 2018). To address concerns about potential secondary contamination by DIG, we proceed to discuss relevant results from the literature. Recently, in this context, Kumari et al. (2019) established a metallicity prescription for DIG- and LI(N)ER-dominated regions. Exploiting Multi Unit Spectroscopic Explorer (MUSE) observations at 50–100 pc scale resolution in 24 nearby star-forming galaxies, the authors selected a sample of individual DIG/LI(N)ER – H II region pairs located sufficiently close to each other to be assumed to share a single metallicity. In particular, the study encouragingly found the O3N2 diagnostic (based on H α, [N III] λ6583, H β, and [O III] λ5007) to be remarkably robust in DIG/LI(N)ER regions, showing only a minor offset of <0.04 dex from the ground truth derived in the H II regions, with 0.05 dex scatter in either direction. Seyfert-classified spaxels located in the outskirts were also included in the analysis.

On the topic of possible DIG contamination, a similar conclusion was reached by Vale Asari et al. (2019) for a set of ∼1400 MaNGA galaxies, with the additional challenge that the ∼kpc scale resolution does not allow resolving individual H II regions. For a careful exploration of how a loss of spatial resolution can impact and smoothen recovered metallicity gradients, we refer the reader to Mast et al. (2014). Vale Asari et al. (2019) used high-S/N star-forming spaxels and characterized the contribution of DIG to relevant emission lines via the equivalent width of the H α line. The latter has been favoured as a tracer of DIG over the H α surface brightness, since it assesses how faint the line emission is relative to the underlying stellar continuum (rather than in absolute terms) and can therefore identify multiple DIG regions stacked along the line of sight (Lacerda et al. 2018). The work by Vale Asari et al. (2019) concluded that the O3N2 metric was not significantly affected by DIG contamination (while a moderate impact was recovered for N2 based on [N II]/Hα). On the other hand, an earlier study by Zhang et al. (2017) analysed 365 face-on star-forming MaNGA galaxies, and found the O3N2 index to be biased in DIG-dominated regions identified by their low H α surface-brightness density (with the abovementioned caveat). However, they also found the associated bias in O3N2-based metallicity gradients to be limited to ± 0.05 dex/R_e in either direction. Due to the symmetric character of the bias, one can argue that given sufficient number statistics, any DIG contamination could thus not cause any artificial correlations of the gas-phase metallicity gradient with other galaxy properties, but merely weaken any existing trends at worst.

Going back to LINER emission, we note that in LINERs with low Hα equivalent width thought to be photoionised by post-AGB stars rather than AGN (Binette et al. 1994; Singh et al. 2013), Oliveira et al. (2022) favoured the N2 ([N II]/ H α-based) metallicity calibrator over O3N2, motivated by photoionization models of post-AGB (post-asymptotic giant branch) populations. However, in this work, we will select only LINERs whose H α equivalent width suggests them to be ionized by an AGN as discussed in the next Section 2.5, and the considerations on potential DIG contamination outlined above may further disfavour N2.

All things considered, the literature reinforces our confidence in applying the O3N2 metallicity diagnostic taken from the Pipe3D catalog as discussed in Section 2.3.2 to galaxies showing DIG emission, especially given that the Pipe3D metallicity gradients are calculated using only star-forming regions within these sources (and excluding the central 0.5 R_e). Further, while observational studies investigating the impact of LI(N)ER emission on different metallicity calibrators are still sparse to date, the abovementioned results of Kumari et al. (2019) motivate us to also explore O3N2-derived metallicity gradients within the LINERs, Seyferts, and Composites in the MASCOT sample, which we dub 'AGN-like' objects. We note that, while the majority of our AGN-like objects are not classified as Seyferts, it has been cautioned against using the O3N2 metallicity prescription in Seyfert AGN due to its sensitivity to ionisation – the theoretical predictions in Kewley et al. (2019) suggest it to vary by

over 2 dex e.g. at solar metallicity when evaluated over an ionization grid spanning 2 dex from log $U = -3.98$ to -1.98 (their fig. 9). In Section 3, we therefore also use the R23 metallicity diagnostic, which Kewley et al. (2019) predict to be robust against ionization at the metallicities spanned by our sample (log O/H > 8.6).

2.5 Sample selection

Motivated by the findings in the previous Section 2.4 on the applicability of the O3N2 metallicity diagnostic in the presence of DIG and LINER emission, we focus on below/on-MS galaxies and include LINERs/Composites/AGN in our sample. In detail, we select our sample as follows:

(i) We start by using the Renzini & Peng (2015) MS prescription to select all targets from the MASCOT (+ ALMaQUEST) sample that fall below the ridge corresponding to the dashed line in Fig. 1. We note that given the intrinsic scatter of the MS of ∼0.3 dex and the uncertainties in SFR and $M_\star$, a significant part of our sample is formally consistent with being on-MS. While we do not define a pure below-MS sample, the average properties of our sample capture those of a less active and transitioning population and can be contrasted against the average properties of those galaxies falling above the MS ridge. Henceforth, we refer to the selected sources as 'below-MS sample' for the sake of simplicity.

(ii) Among these, we exclude edge-on galaxies with $b/a < 0.2$ (for which the limited view on their centres makes metallicity gradients challenging to derive).

(iii) We exclude type I AGN using the Comerford et al. (2020) catalog as host-galaxy properties are challenging to derive in cases where the central QSO outshines its host.

(iv) We further exclude major mergers identified by visual inspection (meaning constellations with two galaxies falling into the ARO beam). In galaxies undergoing a major merger with disturbed morphology, radial profile analyses are complicated by the fact that spaxels at the same distance from the centre may not be directly comparable to each other if the galaxy is disrupted in a non-axisymmetric way. Mergers may moreover affect the metallicity distribution within galaxies via mixing processes and inflows, as we will discuss in more detail in Section 4.4.

(v) Finally, we split our sample to consider separately purely star-forming galaxies and 'AGN-like' objects that include LINERs, Composites, and Seyferts. The latter are identified via the N II and S II Baldwin, Phillips & Terlevich (BPT) diagram (Kewley et al. 2001; Kauffmann et al. 2003) using the line ratios extracted from a circular aperture of 1 kpc around the centre. For spaxels that fall only partially within the circle, we use weights as the fraction of their area which belongs to the circle. We further exclude spaxels that are flagged as unusable by the MaNGA DAP ('DONOTUSE' flag[2]), as well as those with S/N<3 for any of the BPT lines or with negative line fluxes. Finally, we follow Sánchez et al. (2018) by requiring AGN-like objects to have an Hα equivalent width above 1.5 Å (to remove LINERs photoionized by post-AGB stars rather than AGN). The methodology will be further detailed in an upcoming paper (Albán et al., in preparation).

We discard galaxies that were undetected in our CO observations. Our final sample thus selected contains 79 galaxies. Among these, 38 are LINERs/Composites/Seyferts and 41 are inactive galaxies.

3 RESULTS

3.1 A link between gas-phase metallicity gradients and depletion times in AGN-like galaxies below/on the MS

For the optically selected type 2 AGN, LINERs, and Composites *below/on the MS* from our sample described above in Section 2.5, we find a relation between gas-phase metallicity gradients ∇Z and molecular gas depletion times $t_{\rm dep} = M_{\rm H_2}/{\rm SFR}$, which is shown in Fig. 2 in the top panel. The correlation is strong with an associated p-value of ∼0.001 and r-value of 0.56, as annotated in the top of the figure together with the best linear fit (slope: 0.07 ± 0.02). When excluding the data point with longest $t_{\rm dep}$, the statistical coefficients are merely changed to $p = 0.003$ and $r = 0.52$. We report that such a relation is not present *above the MS* (Fig. A1 in the appendix). In Fig. 2, the Seyfert AGNs are coloured in black, while the LINERs and Composites are shown in purple, and for CO non-detections, upper limits are indicated via an arrow (but not included in the analysis). The best-fitting relation is overplotted as a black line and the red lines represent uncertainties on the fit. The latter are obtained via MCMC-sampled fits from the `linmix` module,[3] which repeatedly perturbs the data points within their uncertainties and reruns the fitting. Each such fit yields slightly different coefficients, and the median coefficients over all iterations are used to define the best-fitting relation.

As a further statistical check, we validate the robustness of the correlation by constructing 1000 bootstrapped samples that are drawn from the observed sample with replacement and using them to calculate a distribution of r-values. The latter peaks at $r = 0.55$, and we confirm that it does not contain $r = 0$ in its associated 95 per cent confidence interval (Appendix B). On a different note, we point out that Fig. 2 displays depletion times based on the metallicity-dependent CO-to-H_2 conversion outlined in Section 2.1, but we will address and test that assumption in Section 3.2.

Moving to inactive galaxies, the middle panel of Fig. 2 displays the ∇Z–$t_{\rm dep}$ plane for those system that show no optical signs of LINER or AGN character in their central spaxels according to the BPT selection. In this case, we find no evidence for a correlation (although the picture could conceivably change when increasing the number statistics after a future MASCOT data release).

As mentioned in Section 2.4, the applicability of the O3N2 metallicity prescription is not guaranteed in Seyfert AGN given the calibrator's sensitivity to ionization. On the other hand, Kumari et al. (2019) found the diagnostic to be very robust in LINERs and DIG regions based on studying H II-DIG/LI(N)ER pairs in nearby spirals (as well as including non-central Seyfert-classified regions). In Section 3.2, we will conduct a sanity check using a different metallicity diagnostic. For now, in the bottom panel of Fig. 2, we show the relation excluding Seyfert AGN and focusing on LINERs/Composites only. The correlation coefficient $r = 0.54$ and p-value $p = 0.005$ still support a strong correlation. We also checked that the correlation is still significant with $p = 0.017$ when excluding both the Seyferts and the single data point with the longest depletion time. The ∇Z–$t_{\rm dep}$ relation therefore does not depend on the inclusion of type 2 Seyfert AGN.

The depletion time $t_{\rm dep} = M_{\rm H_2}/{\rm SFR}$ on the x-axis is inversely related to how efficiently a galaxy is converting its remaining H_2 gas into stars. It is thus an important quantity in galaxy evolution, particularly in the below-MS regime, where one may simplistically

[2] https://sdss-mangadap.readthedocs.io/en/latest/metadatamodel.html

[3] https://linmix.readthedocs.io/en/latest/

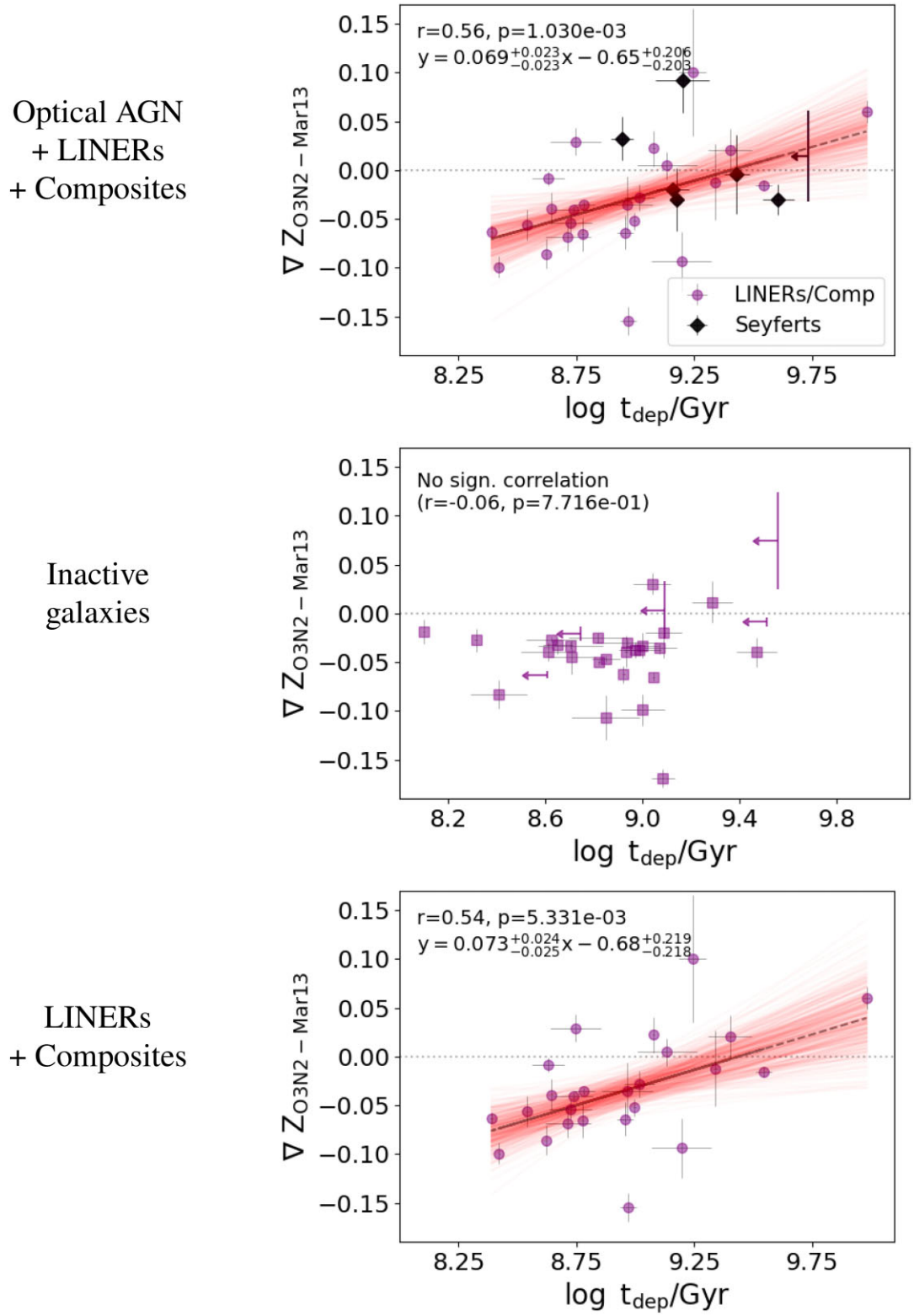

Figure 2. Metallicity gradients ∇Z as a function of depletion time $t_{\rm dep} = M_{\rm H_2}/{\rm SFR}$ below the MS. *Top panel*: Relation for AGN, LINERs, and Composites. Seyfert AGN are highlighted in black, whereas LINERs and Composites are shown in purple. *Middle panel*: For the inactive galaxies in our sample, we find no correlation. *Bottom panel*: Relation for LINERs and Composites – discarding AGN due to concerns about the applicability of the O3N2 metallicity prescription, but including LINERs given the robustness of the O3N2 calibration. In the top and bottom panels, the best-fitting relation is overplotted as a black line, with uncertainties illustrated by the red transparent lines. Upper limits are shown by arrows and excluded from the analysis. The correlation is significant in all panels except for the inactive galaxies (see annotated p-values and r-values). It further holds when excluding the data point with longest $t_{\rm dep}$ in the top and bottom panel with $p = 0.003/0.017$ and $r = 0.52/0.48$, respectively. We here use gas-phase metallicity gradients based on the O3N2 diagnostic and calculate $t_{\rm dep}$ based on a metallicity-dependent CO-to-H_2 conversion $\alpha_{\rm CO}$. However, we revisit the relations in this figure from Figs 6 and 7, where we use a constant $\alpha_{\rm CO}$ and a different metallicity calibrator as a sanity check.

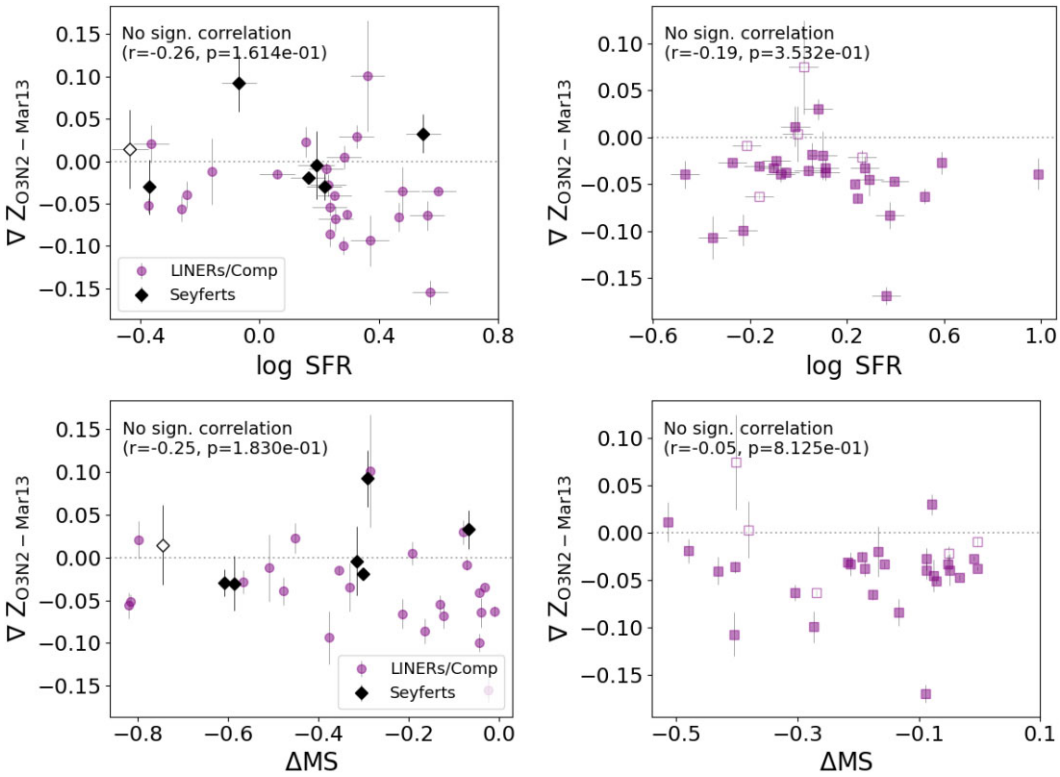

Figure 3. Metallicity gradients plotted against SFR values in the top row and against MS offset $\Delta\mathrm{MS} = \log\ \mathrm{SFR} - \log\ \mathrm{SFR}_{\mathrm{RP15}}$ in the bottom row. In the left column corresponding to AGN, LINERs, and Composites, the optically selected Seyfert AGN are highlighted in black, while the purple data points correspond to LINERs and Composites. The right-hand panels focus on inactive galaxies instead. In active and inactive panels alike, we report no correlation between ∇Z and SFR, nor between ∇Z and ΔMS. We thus conclude that we cannot trace back the ∇Z–t_{dep} relation from Fig. 2 to a pure relation with SFR or MS offset. Instead, variations in ∇Z are primarily driven by t_{dep} (relation in Fig. 2).

interpret it as a measure of how quenched a system is, though the picture becomes more complicated when considering that not all systems below the MS are indeed in the process of being quenched – some may conceivably move back to the MS in the future following SFR fluctuations (see e.g. Chauke et al. 2019 for rejuvenation events in LEGA-C galaxies). Within this context, Colombo et al. (2020) recently used resolved molecular gas properties and optical-IFU data from the EDGE-CALIFA survey to compare centrally star forming and centrally quenched galaxies. While this type of analysis is complicated by CO-non-detections, their findings suggest that once galaxies are moved below the MS due to a central shortage of molecular gas, the depletion time then becomes the main driver that pushes them further towards quiescence when they are already gas-poor and centrally quenched. The relation we find in Fig. 2 thus supports a picture in which any mechanism(s) that quench AGN-like galaxies also flatten or invert metallicity gradients in the process.

We note that the existence of a ∇Z–t_{dep} relation is in qualitative agreement with recent findings from Sánchez et al. (2021a). These authors used optical dust attenuation as a tracer to derive molecular gas mass estimates (see Concas & Popesso 2019) for a compilation of publicly accessible IFU data sets. They also explored the behaviour of both the star-forming efficiency SFE and metallicity gradients as a function of mass for different morphological types (their Fig. 16). While both quantities show a negative dependence on mass for the general population (which would *a priori* suggest a positive correlation between ∇Z and SFE), the results strongly depend on morphology. In particular, for intermediate-type galaxies that are located preferentially below the MS (such as S0), the trend between mass and ∇Z inverts, which suggests ∇Z to be inversely correlated with SFE in these objects, and thus positive correlated with the depletion time t_{dep}. Our findings are thus qualitatively consistent with the results from Sánchez et al. (2021a) based on indirect molecular gas estimates. We will revisit the role of morphology in Section 4.5.

Given the observed link between longer depletion times and declining star-forming activity below the MS (e.g. Saintonge et al. 2017, Wylezalek et al. 2022), it is instructive to contrast the metallicity gradients also against SFRs and MS offsets instead of depletion time. In the top panels of Fig. 3, we look for a relation between ∇Z and SFR, with AGN/LINERs/Composites shown in the left-hand panel and inactive galaxies in the right-hand panel. In the left-hand panel, the black symbols denote BPT-selected Seyfert AGN, while the purple dots show LINERs and Composites. Galaxies that are CO-undetected are shown via open symbols. We note that while we use the Pipe3D SSP-derived SFR values in this plot, the associated SSP-derived errors are likely to be underestimated since they merely describe how easily a best-fitting SFR value can be found among all templates. We therefore choose to use Hα-derived uncertainties. Both for active and inactive galaxies alike, there is no evidence for a correlation between ∇Z and SFR. We will, however, revisit the impact of star formation in a resolved fashion in Section 4.2.

In the bottom panels of Fig. 3, we also contrast the ∇Z values to the MS offset $\Delta\mathrm{MS} = \log\ \mathrm{SFR} - \log\ \mathrm{SFR}_{\mathrm{RP15}}$ with respect to the Renzini & Peng (2015) prescription for the MS, again finding no correlation for active (*left-hand panel*) and inactive (*right-hand panel*) galaxies alike. In Section 4.5, we further show that the metallicity gradients are not correlated with the amount of molecular

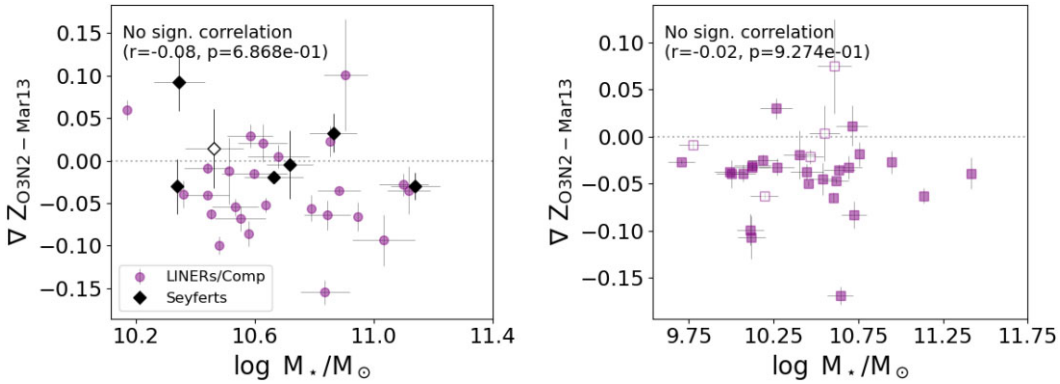

Figure 4. Metallicity gradients ∇Z plotted against stellar mass $M_\star$. We do not find any correlation in either AGN/LINERs/Composites (left-hand panel) or inactive galaxies (right-hand panel), so we conclude that mass effects cannot explain the ∇Z–$t_{\rm dep}$ relation found in Fig. 2.

gas within our sample. These findings indicate that the metallicity gradients are primarily driven by the depletion time rather than SFR or MS offset. Thus, the crucial factor is not the absolute star formation, but rather the level of star formation in relation to how much building material is still left in the form of cold molecular gas.

Finally, it is necessary to check for the presence of mass effects among subsamples that may impact our results. In particular, we note that as can be seen in Fig. 1, the AGN/LINERs/Composites in our sample have somewhat higher stellar masses than the inactive galaxies on average, which could *a priori* complicate a direct comparison between them. For those galaxies that pass our selection criteria, we find that inactive galaxies are distributed around a median mass of $\log M_\star = 10.45$ with a spread of 0.37 dex, while the AGN/LINERs/Composites show a median mass of $\log M_\star = 10.63$ with 0.25 dex scatter. Thus, the masses of selected active and inactive are comparable within 1σ. Importantly, in Fig. 4, we show that within our sample there is no correlation between metallicity gradients and stellar mass either for AGN/LINERs/Composites (*left-hand panel*) or inactive galaxies (*right-hand panel*). Thus, we do not suspect that mass effects play a role in the ∇Z–$t_{\rm dep}$ relation in the AGN-like objects in our study.

3.2 Sanity checks investigating potential unphysical drivers of the relation

Before we go into a discussion on possible physical interpretations for the ∇Z–$t_{\rm dep}$ relation presented in Section 3, we will first test the robustness of these results with respect to unphysical drivers including key aspects of our adopted methodology.

First, we search for potential inclination effects affecting our analysis in Fig. 5 by contrasting the metallicity gradients to the minor-to-major axis ratio b/a for AGN-like objects (left-hand panel; with Seyferts highlighted in black) and inactive galaxies (right-hand panel). CO-undetected galaxies are shown as open symbols. Encouragingly, we clearly do not find any correlation between ∇Z and b/a. We therefore do not expect inclination effects to play a significant role in our analysis.

Further, it is important to note that in Fig. 2, the x- and y-axes – $t_{\rm dep}$ and ∇Z – are not fully independent of each other. The molecular gas masses entering $t_{\rm dep}$ are derived from our observed CO fluxes using the $\alpha_{\rm CO}$ conversion factor from Accurso et al. (2017; see Section 2.1), which depends on galaxy-integrated metallicity (as well as offset from the star-forming MS). It is therefore necessary to check how our results may vary when using a constant $\alpha_{\rm CO}$ factor to derive H_2 masses and associated depletion times. In Fig. 6, we use a constant value of 4.36 $M_\odot/(K\,km\,s^{-1}\,pc^{-2})$ for $\alpha_{\rm CO}$ corresponding to the canonical Milky Way value, and plot the resulting ∇Z–$t_{\rm dep}$ relation in an analogous way to Fig. 2. For the AGN/LINERs/Composites (left-hand panel) and LINERs + Composites (right-hand panel), we still obtain a significant ∇Z–$t_{\rm dep}$ relation with similar slopes than in Fig. 2 (as well as no relation for inactive galaxies in the middle panel). Throughout the rest of the paper, we will continue using the metallicity-dependent $\alpha_{\rm CO}$ factor to derive depletion times and other molecular gas properties.

As a second check, we verify that our results do not depend entirely on our choice of metallicity prescription. For this, we explore using gas-phase metallicity gradients from the Pipe3D catalog based on the Tremonti et al. (2004) R23 calibration instead of the Marino et al. (2013) O3N2 diagnostic, since the former has been shown to be practically insensitive to the ionization parameter U in the regime with $\log(O/H) + 12 > 8.5$ when evaluated over $-3.98 < U < -1.98$ (Kewley et al. 2019). We retrieve a metallicity range of $8.62 < \log(O/H) + 12 < 8.89$ for all galaxies passing our sample selection. We show the resulting ∇Z–$t_{\rm dep}$ relation based on the R23 calibrator in Fig. 7, where the left-hand panel again corresponds to AGN + LINERs + Composites, the middle panel to inactive galaxies, and the right-hand panel to LINERs + Composites. In all cases except for the inactive galaxies, we recover a significant correlation. Interestingly, compared to Fig. 2, we obtain a significantly steeper slope (0.22 versus 0.07 Gyr^{-1}). However, we choose to proceed with the metallicity gradients obtained via the Marino et al. (2013) O3N2 method, given that many of our galaxies are affected by DIG and/or LINER emission, in which the robustness of the O3N2 calibrator has been tested as summarized in Section 2.4 (while such a test has, to our knowledge, not been conducted for R23).

4 DISCUSSION

In this section, we will discuss various interpretations of the origin of the ∇Z–$t_{\rm dep}$ relation presented in Section 3.1.

4.1 Outflow scenario

The metallicity gradients within galaxies are responsive to internal galaxy processes as well as gas accretion and feedback. In this section, we consider the scenario of metal-enriched outflows redistributing metals and facilitating chemical mixing within galaxies. In this picture, we hypothesize that the below-MS galaxies with longer

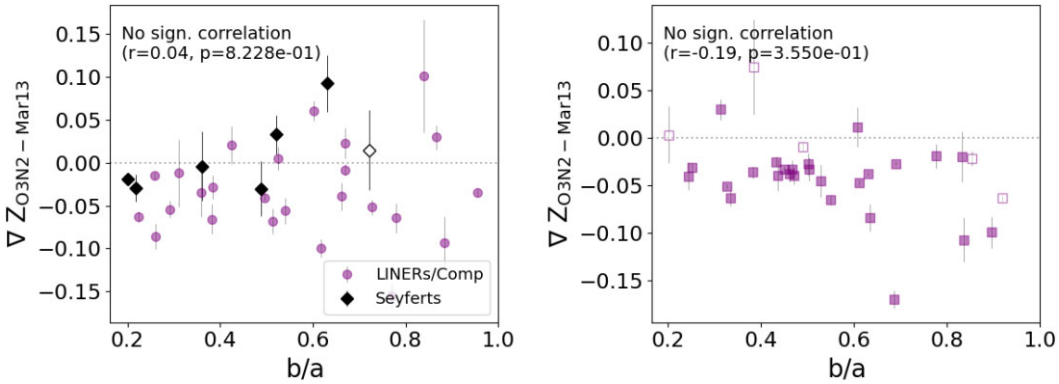

Figure 5. Gas-phase metallicity gradients ∇Z plotted against the minor-to-major axis ratio b/a. In the left-hand panel focusing on AGN/LINERs/Composites, Seyferts are highlighted in black. The right-hand panel corresponds to inactive galaxies. The open symbols denote CO-undetected sources. In either case, we do not find any correlation between ∇Z and b/a, which argues against inclination effects affecting our analysis.

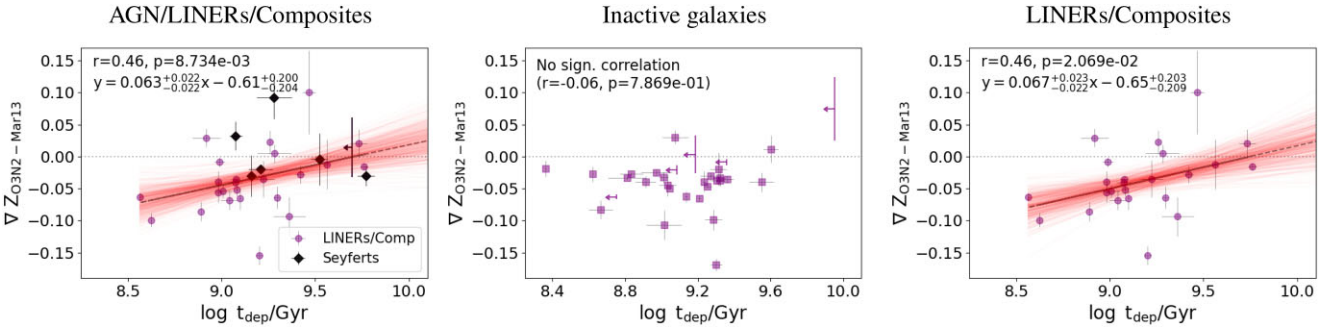

Figure 6. Same as Fig. 2, but recalculating the depletion time with a constant CO-to-H_2 conversion factor $\alpha_{CO} = 4.36\ M_\odot/(K\,km\,s^{-1}\,pc^{-2})$ corresponding to the canonical Milky Way value.

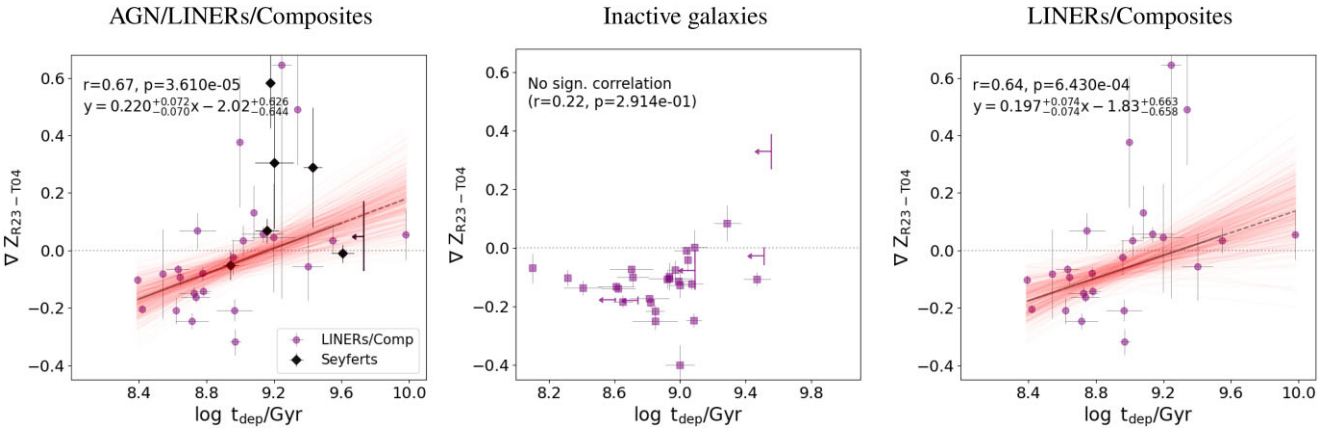

Figure 7. Same as Fig. 2, but using the Pipe3D gas-phase metallicity gradients based on the Tremonti et al. (2004) R23 calibrator instead of the Marino et al. (2013) O3N2 prescription.

depletion times in our Fig. 2 show flatter metallicity gradients as they are (simplistically) at a later evolutionary stage, such that feedback has been operating for a longer time than in those galaxies with short t_{dep} that are efficiently forming stars.

4.1.1 Background

Observational outflow studies have traditionally had a strong focus on the most luminous AGN and starbursts; in recent years, however, ionized outflows have been shown to be present in LINERs (e.g. Cazzoli et al. 2018; Hermosa Mu∼noz et al. 2022), low-luminosity AGN, as well as 'typical' star-forming galaxies (e.g. López-Cobá et al. 2019, 2020), though with limited impact as assessed via coupling efficiency or mass outflow rates (Wylezalek et al. 2020; Avery et al. 2021). In particular, in the context of AGN feedback, it has been suggested that it is the integrated effect over time that makes galaxies quench since black hole mass estimates have been found to hold the most predictive power over galaxies' quenching status (Bluck et al. 2020; Piotrowska

et al. 2022). In this sense, outflows below the MS – despite being likely weak – could be the 'final straw' that pushes galaxies towards quiescence after having been subjected to gas removal/heating on long time-scales via repeated energy injection. In the context of stellar feedback, from a simulations perspective, Gibson et al. (2013) find that even weak SN feedback leads to efficient gas mixing on cosmological time-scales as manifested by a flattening of metallicity gradients towards low redshifts in the MUGS suite (Stinson et al. 2010) of cosmological zoom-in simulations, while stronger feedback produced flat metallicity gradients throughout cosmic time. The adiabatic blastwave model feedback used in these results operates via thermal energy injection into the gas surrounding stellar particles (with the 'strong' model given twice the heating power of the 'weak' model, plus radiation feedback). It therefore does not necessarily manifest in terms of strong outflows and may thus be challenging to constrain observationally, but we will nevertheless explore a quick kinematic analysis to see if any outflow signatures can be found. The importance of AGN feedback has further been highlighted in Illustris TNG50 simulations, where Hemler et al. (2021) argue that it likely contributes significantly to the shallow metallicity gradients recovered at low redshift (next to stellar feedback), especially in high-mass galaxies where kinetic mode AGN feedback kicks in. In EAGLE galaxies, Trayford & Schaye (2019) also demonstrate that in mock spaxels with high stellar-mass surface density $\Sigma_\star$, switching on AGN feedback leads to substantially lower local metallicities (their fig. 7). The strength of the effect was found to depend on $\Sigma_\star$, such that within a given galaxy, one would expect the denser central regions to be most affected.

Metal-enriched outflows on galactic scales have been invoked across redshifts to reproduce the observed chemistry of the circum-galactic medium (see the review by Tumlinson, Peeples & Werk 2017). At low redshift, there have also been observational hints that feedback mechanisms may play a strong role in shaping the metallicity distribution within galaxies. For instance, Baker et al. (2022a) investigate the predictors of resolved metallicities in star-forming MaNGA galaxies, and find intriguingly that there is a stronger anticorrelation with global SFR than with the local SFR (though both local and global quantities matter), which is broadly consistent with large-scale stellar feedback-driven winds ejecting or redistributing metals. Avery et al. (2021) further find evidence for an enhanced dust attenuation within the outflows of MaNGA galaxies, which could potentially be traced back to metal enrichment, while Chisholm, Tremonti & Leitherer (2018) confirmed the high level of metal enrichment in the outflows of seven local star-forming galaxies using spectra from the Cosmic Origins Spectrograph aboard the Hubble Space Telescope (HST/COS).

4.1.2 Kinematic analysis

In light of the considerations above, as a first step, we are searching for kinematic signatures of ouflows in the [O III] line tracing ionized gas. First, we use the [O III] maps from the MaNGA DAP and impose a signal-to-noise threshold S/N > 3.[4] We further discard galaxies in which less than 10 per cent of spaxels fulfill the aforementioned criteria. In each selected spaxel, we then calculate W_{80}, defined as the spectral width that encompasses 80 per cent of the total line flux. For this purpose, the line profiles are fit with a single or double Gaussian, where a second component is only permitted if it has a signal-to-noise S/N > 3 to prevent noise fitting. Skylines are masked. We then calculate the weighted average W_{80} value over all spaxels falling within a circular aperture of radius $0.1R_e$, where each spaxel is weighted by the fraction of its area that falls into the annulus. The methodology will be described in more detail in an upcoming paper investigating kinematic signatures in different types of AGN (Albán et al., in preparation).

In the left-hand panel of Fig. 8, we first attempt to identify indications of kinematic feedback by AGN, stars, or a combination thereof in the more central regions by contrasting the metallicity gradients to the mean [O III] W_{80} within $1\,R_e$ for our sample of AGN-like galaxies. Grey dots show the location of galaxies that were discarded due to less than 10 per cent of their spaxels fulfilling our selection criteria outlined above, and are excluded from the correlation analysis. Black data points denote Seyfert AGN, while LINERs/Composites are shown in purple. There is a significant correlation of central [O III] line width with $r = 0.66$ and $p \sim 0.013$, such that the AGN-like systems with broader lines have flatter or positive metallicity gradients. Given the link we found between ∇ Z and depletion time, we expect $W_{80}(< 1\,R_e)$ to correlate with $t_{\rm dep}$ as well, which we confirm in the right-hand panel of Fig. 8 ($r = 0.84$, $p < 0.001$). For both relations in Fig. 8, we draw 1000 bootstrapped samples from the original data points with replacement and calculate 1000 associated r-values, and verify that the 95 per cent confidence intervals on r do not include zero (Appendix B). We also check that the $\nabla Z - W_{80}(< 1\,R_e)$ relation persists when using a different metallicity diagnostic or a constant CO-to-H_2 conversion factor (Appendix E).

We interpret these findings as a strong indicator of a causal link between outflows (which could be stellar or AGN-driven) and the chemical distribution in our sample of AGN-like objects, as well as star-formation efficiency. We argue again that although one may naïvely expect more massive galaxies to have broader W_{80} values, the trend between ∇Z and $W_{80}(< 1R_e)$ cannot be explained by obvious mass effects, given that we found no relation between ∇Z and stellar mass in Fig. 4 (Section 3.2), although we will discuss the influence of the gravitational potential further in the paragraph below. For now, we highlight that we checked that the same trend is not seen in inactive galaxies (which should in principle show potential well effects similar to the AGN-like objects). We note that this finding does not necessarily imply that the outflows are traced back to AGN feedback with no contribution from stars. We also note that the W_{80} values fall below < 500 km s^{-1} and would thus not be regarded as outflow signatures in studies of galaxies on the MS. However, below the MS, we expect signatures to weaken for both stellar and AGN feedback, as AGN fuelling decreases given a shortage of gas, which is also reflected in the fact that the majority of our below-MS AGN-like objects are LINERs/Composites rather than Seyferts. As outlined above, weak feedback may still play a significant role in this regime. We thus favour an interpretation in which weak outflows may not be trivial to detect when using line widths as a tracer, but still exist.

Before expanding the kinematic analysis, we first address the point that emission line widths are not a pure tracer of outflows, but are expected to also respond to the potential well. The MaNGA spaxels in which we derive [O III] W_{80} values sample a finite range in radii and thus a spread of orbital velocities, and beam smearing may further complicate the picture, with both of these effects being a function of inclination. The correlation seen in Fig. 8 above is therefore likely influenced to some extent by potential well effects. All other factors being equal, galaxies with a higher dynamical mass within the central $1\,R_e$ would experience a stronger line broadening (assuming a fixed

[4]While discarding spaxels with a 'DONOTUSE' flag, as well as negative fluxes.

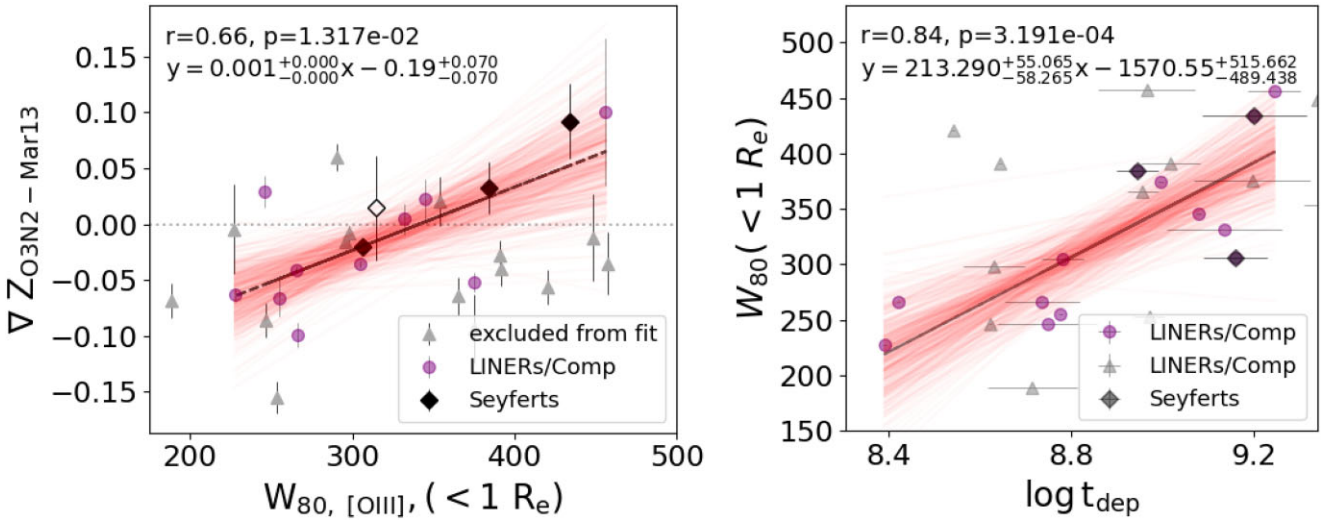

Figure 8. *Left-hand panel*: Gas-phase metallicity gradients ∇Z plotted against the mean [O III] $W_{80}(< R_e)$ parameter (averaged over all spaxels out to 1 R_e). We find a strong correlation between ∇Z and average [O III] W_{80} in Seyfert AGN (black data points) and LINERs/Composites (purple dots). We suggest that this relation emerges via weak chemically enriched outflows. The targets plotted in grey are excluded from the fit due to exhibiting too many spaxels in which we deem the recovered W_{80} values to be unreliable ($S/N < 10$, 'DONOTUSE' flag, or negative flux). Only targets with >10 per cent of reliable spaxels are included in the fit. The best linear fit is shown as a black solid line, while the red lines show fits recovered when perturbing the data points within their uncertainties. The r-value, p-value, and coefficients of the best fit are further annotated in the top of the panel. *Right-hand panel*: There is also a strong correlation between [O III] $W_{80}(< R_e)$ and depletion times t_{dep}, such that the AGN-like galaxies with the strongest [O III] line broadening are the least efficient at forming stars out of the available molecular gas.

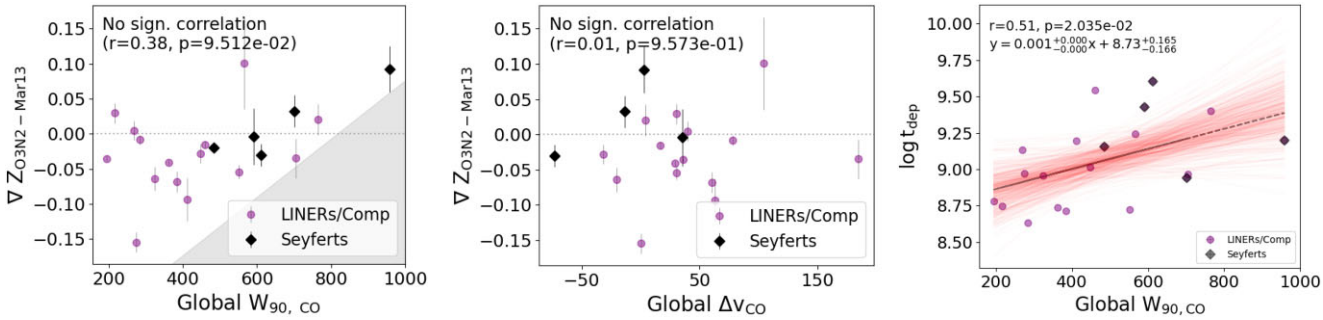

Figure 9. *Left-hand panel*: Metallicity gradients plotted against the W_{90} measurement of the CO line width from the galaxy-integrated CO profiles of our AGN, LINERs, and Composites. *Middle panel*: Metallicity gradients plotted against the median velocity offset between the peak of our galaxy-integrated CO profiles and the frequency predicted for a CO emitter at the exact systemic velocity of a given galaxy (i.e. 115.27 GHz at rest frame). *Right-hand panel*: Depletion times contrasted against the global CO W_{90} values. While we find a possible correlation that could hint at molecular outflows reducing the star-formation efficiency, we caution that given the unresolved character of the CO measurements, the data points with CO $W_{90} < 500$ km s^{-1} are likely driven to a significant extent by the potential well. If one were to remove that contribution, all data points would be shifted to lower W_{90}, especially the low-W_{90} ones.

spaxel size). According to the resolved mass-metallicity relation (Rosales-Ortega et al. 2012; Sánchez et al. 2013; Barrera-Ballesteros et al. 2016), more concentrated galaxies would broadly be expected to have higher central metallicities (though with a large scatter), which may simplistically translate into more negative metallicity gradients. In this case, one may naïvely expect an anticorrelation between ∇Z and W_{80} in active and inactive galaxies alike, unlike the positive correlation we find in Fig. 8 in AGN-like objects only. Further, we found no mass dependence nor inclination dependence of the metallicity gradients (Figs 4 and 5). In Section 4.5, as well as the Appendix D focusing on morphological tracers, we will see that we do not find evidence for any correlation between ∇Z and the stellar mass surface density , nor with the central stellar or Hα velocity dispersions (top row of Fig. D1). In the appendix (Section C), we search more directly for potential dependencies of the W_{80} parameter, but find no evidence for any trend with stellar mass, stellar-mass surface density, or inclination (Fig. C1). We therefore interpret [O III] W_{80} as being primarily a tracer of outflows.

To explore a possible impact of feedback (AGN or stellar) on global scales, we contrast the metallicity gradients against the galaxy-integrated [O III] W_{80} (median over all selected spaxels) for our AGN/LINERs/Composites. In this case, we report that we do not find any evidence for a correlation ($p = 0.06$; omitted from Fig. 8), though we note that that the possibility of a delayed impact cannot be excluded.

We then proceed to study the cold gas kinematics of the AGN-like objects in Fig. 9. In the left-hand panel, we plot the metallicity gradients as a function of the W_{90} value obtained from our galaxy-integrated velocity profiles, i.e. the width containing 90 per cent of the CO line flux (which is more sensitive than W_{80} for narrow CO line profiles with coarse spectral bins spanning $\sim$ 50km s^{-1}). The CO line is fitted by a single or double Gaussian as required, as outlined

in Wylezalek et al. (2022). We do not find any significant relation, although we note an 'empty triangle' region shaded in grey such that no objects fall into the regime with large W_{90} and substantially negative ∇Z. We note that the galaxy-integrated character of our CO measurements implies that the CO W_{90} is expected to be dominated by the potential well for those objects showing low line widths. Those data points with $W_{90} \gtrsim 500$ km s^{-1}, however, are unlikely to be solely driven by the rotation of the galaxy, and may exhibit potential indications for a ∇Z–W_{90} correlation, which is however not possible to verify given the low number statistics in this regime. We further find no relation in the middle panel of Fig. 9 when contrasting the metallicity gradients to the velocity offset between our observed CO line peak and the line predicted for a CO emitter at the exact systemic velocity of a given galaxy (i.e. 115.27 GHz at rest frame). Finally, we note that when contrasting the CO W_{90} measurements against depletion times (instead of metallicity gradients as in the first panel), a potential relation arises, but we caution again that especially the systems with low W_{90} are expected to be strongly driven by the spread in orbital velocities contained within the entire galaxy (with gas moving both towards and away from an observer). If the relation was shown to persist when removing the contribution of the rotation curve to W_{90} e.g. by modelling galaxies as inclined rotating discs (which should strongly decrease the low-W_{90} values in particular), this would be evidence for molecular gas outflows reducing the star formation within AGN-like galaxies. However, we defer a more in-depth study of the CO kinematic profiles to a future analysis. We further checked that in inactive galaxies, there is no relation between global cold gas kinematics and metallicity gradients or $t_{\rm dep}$. We note that our single-dish observations do not allow us to explore resolved kinematics of the neutral gas phase, and molecular outflow signatures are more challenging to detect on a global scale.

To conclude this section, considering the [O III] ionized gas kinematics in AGN-like galaxies in Fig. 8, we suggest that low-velocity outflows (of stellar or AGN origin) below the MS could plausibly drive chemical mixing in AGN/LINERs/Composites while prolonging depletion times (i.e. reducing star-forming efficiency) and possibly driving those galaxies towards quiescence in a 'last straw' scenario. Our findings raise the question of how metal-mixing time-scales compare to AGN lifetimes. AGNs have been suggested to 'flicker' on and off in many consecutive short cycles of $\sim 10^5$ yr amounting to a total lifetime of 10 Myr–1 Gyr as estimated from e.g. the Soltan argument (Schawinski et al. 2015). However, it is not clear *a priori* how the outflow strength in AGN varies across their lifetime. Our naïve assumption is that the galaxies with stronger outflow signatures in Fig. 8 (and flatter/positive metallicity gradients) are 'older' to allow more time for metal redistribution, though the exact time required for that is also challenging to constrain. For instance, using a toy model describing metal production based on the observed SFR density profiles of $z \sim 1$ galaxies, Simons et al. (2021) argue that in the absence of any redistribution mechanism, galaxies would develop rapidly declining metallicity gradients incompatible with observations on time-scales of $\sim 10 - 100$ Myr, which may thus be regarded as an upper limit to metal-mixing time-scales.

4.2 Connection to fluctuations in local star-forming activity

It is well-established that the global metallicities of galaxies are linked to both global stellar mass and SFR (the 'fundamental metallicity relation'; Ellison et al. 2008, Mannucci et al. 2010). It has further been proposed that this global relation arises from local scalings between the resolved stellar mass, SFR, and oxygen abundance. In particular, Sánchez et al. (2021a) show mathematically that once a local relation is in place, a global one naturally follows. Barrera-Ballesteros et al. (2016) confirm the existence of a local mass–metallicity relation (see also Rosales-Ortega et al. 2012; Sánchez et al. 2013), while they find no evidence for a secondary relation with SFR surface density $\Sigma_{\rm SFR}$, similarly to Alvarez-Hurtado et al. (2022). On the other hand, Sánchez Almeida & Sánchez-Menguiano (2019) and Baker et al. (2022a) report a local anticorrelation between $\Sigma_{\rm SFR}$ and metallicity at fixed mass in MaNGA galaxies (see also the review by Maiolino & Mannucci 2019). This has been attributed to localized inflows fuelling star formation whilst diluting the enriched gas, though Baker et al. (2022a) highlight the even stronger importance of the global SFR in setting local metallicities. The significance of the global SFR could possibly be attributed to the transport of metals by galactic-scale winds driven by stellar feedback.

In this section, we explore the possibility that the ∇Z–$t_{\rm dep}$ relation may arise due to variations in local *in situ* star formation, which simultaneously link to the resolved metallicities and affect the local depletion time $t_{\rm dep} = M_{\rm H_2}/{\rm SFR}$. To evaluate variations in SFR whilst controlling for stellar mass, we derive the radially resolved $\Sigma_{\rm SFR}$-$\Sigma_\star$ distribution for our below-MS sample as follows. We subdivide each galaxy in our sample into annuli of $0.2\,R_e$ width and run our full spectral fitting procedure (described in Section 2.3.3 along with a comparison between our recovered global SFR & $M_\star$ and the Pipe3D reference values) on the annular spectra. We thus recover the SFR surface density and stellar mass surface density in individual annuli, which we show as a scatter plot in the left-hand panel of Fig. 10 for our AGN-like objects, with the median baseline shown as a red solid line. Both quantities have been deprojected.

We then proceed to calculate, for each AGN/LINER/Composite, the radial profile of the offset $\Delta\Sigma_{\rm SFR}$ between $\Sigma_{\rm SFR}$ and the median value at fixed mass ($\langle\Sigma_{\rm SFR}(\Sigma_\star)\rangle$) in our sample, and analyse how they vary as a function of depletion time. In the middle panel of Fig. 10, we classify the resulting profiles in two bins according to their metallicity gradient, as indicated by the colour (green/purple = negative/positive ∇Z). The dashed lines indicate the median profile in each $\nabla Z/t_{\rm dep}$ bin, and the shaded regions indicate the spread between profiles. While the spread in profiles is large, there may be a potential indication of elevated star formation (while controlling for mass) in the outskirts of AGN-like galaxies with negative metallicity gradients compared to those with $\nabla Z > 0$, while their centre is already quenched. Given the relation we found between ∇Z and $t_{\rm dep}$, we also inspect the role of the depletion time in setting the $\Delta\Sigma_{\rm SFR}$ profiles in the right-hand panel of Fig. 10. The colour-coding reflects a binning into the upper and lower 50th percentile of $t_{\rm dep}$ values (blue/red = short/long $t_{\rm dep}$). We find a trend with $t_{\rm dep}$ such that objects with longer depletion time (corresponding to positive metallicity gradients) show a suppression of star formation in their outskirts compared to objects with short $t_{\rm dep}$ whilst exhibiting similar levels of star formation in the centre. Within the context of the resolved fundamental metallicity relation, the drop in SFR in the outskirts may drive higher local metallicities at large radii (e.g. via a lack of diluting H_2 gas), thus flattening or inverting gradients compared to AGN/LINERs/Composites with short $t_{\rm dep}$.

It is interesting to note that despite our results on outflows in the previous Section 4.1, the more quenched galaxies with long depletion times and positive ∇Z are more suppressed in star formation in the outskirts than in the centre. The weak character of the outflows may indicate that while they can mix gas efficiently within galaxies, they do not permanently remove it from their centre. In fact, the deficit of star formation in the outskirts is more broadly in line with e.g. radiative feedback scenario heating up the surrounding medium to prevent new inflows (see Brennan et al. 2018 for a prediction of preventative feedback restricting the accretion of diluting gas in

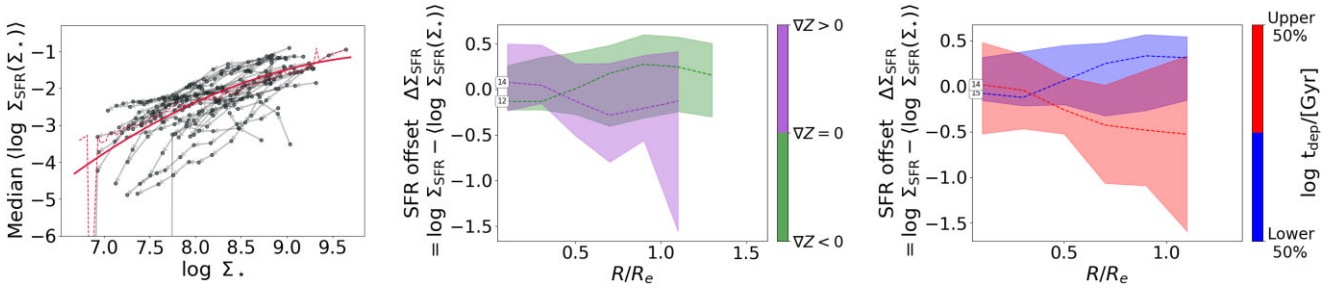

Figure 10. *Left-hand panel*: The individual dots show the $\Sigma_{\rm SFR}$-$\Sigma_\star$ distribution of our AGN/LINERs/Composites sample using annuli of 0.2 R_e width, with the red solid line showing the median SFR surface density $\langle\Sigma_{\rm SFR}(\Sigma_\star)\rangle$ for a given mass. Each grey background curve corresponds to a single galaxy, with each data point on the curve corresponding to an individual annulus, such that the arrows show the path taken in the $\Sigma_{\rm SFR}$–$\Sigma_\star$ plane when going from the centre-most annulus to the outermost one. *Right-hand panel*: Radial profiles of the offset $\Delta\Sigma_{\rm SFR}$ from the median of the $\Sigma_{\rm SFR}$-$\Sigma_\star$ distribution spanned by our sample (solid line in top panels), i.e. offset between SFR surface density $\Sigma_{\rm SFR}$ within a given annulus and the median SFR surface density $\langle\Sigma_{\rm SFR}(\Sigma_\star)\rangle$ evaluated at the stellar mass contained within the annulus. In each panel, the sample is subdivided into galaxies with longer/shorter depletion times (upper/lower 50th percentile of $t_{\rm dep}$), as indicated by red/blue colouring. The dashed lines show the median profile in a given $t_{\rm dep}$ bin, with associated spread illustrated by the shaded regions. The AGN-like objects with long depletion times show a similar central star-forming activity at fixed mass than those with short depletion times, but are comparatively more passive in the outskirts.

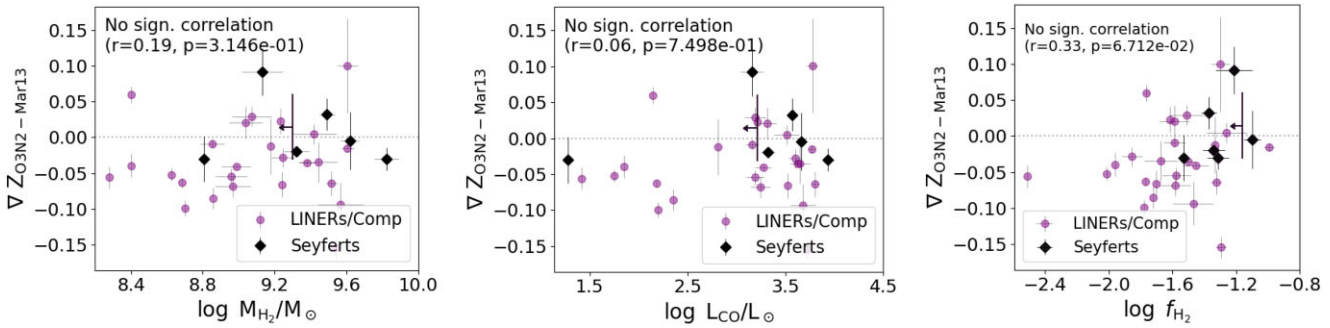

Figure 11. Metallicity gradients plotted against molecular gas mass $M_{\rm H_2}$ (left), CO luminosity (middle), and molecular gas fraction $M_{\rm H_2}/M_\star$ (right). We do not see any correlation in any of these planes.

cosmological zoom-in simulations). For inactive galaxies (omitted from Fig. 10), we could not easily identify any trend with $t_{\rm dep}$ in the shape of Δ ΣSFR profiles that exhibited large spreads.

To summarize, we find a tentative link between positive metallicity gradients and suppressed star formation in the outskirts in AGN-like galaxies, which further coincides with long depletion times. Thus the metallicity gradients of our sample of AGN-like objects may indeed be partially explained by a connection to *in situ* star formation, though our results on the importance of outflows, in the previous Section 4.1, suggest that this is not the whole picture. We conclude for now that in AGN-like objects, the observed ∇Z–$t_{\rm dep}$ relation may arise as a combination of at least two drivers. We proceed to consider other factors (inflows, mergers, and morphological factors) in the following sections.

4.3 Inflow scenario

In this section, we consider the possibility of radial inflows of pristine/metal-poor gas funneled directly to the central regions of galaxies causing flatter/positive metallicity gradients by diluting the central regions in those galaxies that have long depletion times. For nearby galaxies on the MS, Lutz et al. (2021) found local O3N2-based metallicities to be correlated with the galaxy-integrated *atomic* gas fraction. We note that the inflow scenario may not be as straightforward for the galaxies in our sample, given that these all fall below the MS by selection and one may therefore, in general, expect them to be more gas-deficient (e.g. Saintonge et al. 2017). Nevertheless, it is not impossible for galaxies below the MS to contain a significant amount of gas without star formation being fuelled (though this appears to be more often the case for atomic hydrogen, see e.g. Janowiecki et al. 2020). For instance the gas may be stabilized against fragmentation and collapse via morphological transformation (Martig et al. 2009). In Section 4.5, we will discuss potential impacts of morphology in more detail. Here, we explore instead how the metallicity gradients behave as a function of CO luminosity, H_2 mass, and H_2 fraction for our sample to check if there is any direct evidence of recent gas inflows manifesting via an enhanced amount of gas.

In Fig. 11, we contrast ∇Z to the molecular gas mass $M_{\rm H_2}$ in the left-hand panel, to the CO luminosity $L_{\rm CO}$ in the middle panel, and the molecular gas fraction $f_{\rm H_2} = M_{\rm H_2}/M_\star$ in the right-hand panel. In either case, we do not find any evidence for a correlation. For inactive galaxies omitted from Fig. 11, we similarly do not find any evidence for inflows driving the observed metallicity gradients. We note, however, that localized inflows that do not propagate to galaxy-wide scales would be challenging to detect given our unresolved CO observations. Within this context, interestingly, a recent statistical study of the resolved fundamental metallicity relation in MaNGA galaxies (Baker et al. 2022a) found that the strongest predictors of local metallicity were not the local SFR surface density (and local stellar mass surface density), but instead the global SFR and global stellar mass. The fact that the local SFR is only of secondary

importance in setting local metallicities (see also Alvarez-Hurtado et al. 2022) also argues against localized inflows being a primary driver (as inferred via the resolved KS relation; Schmidt 1959; Kennicutt 1998).

4.4 Merger scenario

Aside from *in situ* chemical evolution and metal transport due to inflows or feedback processes, the metallicity distribution within galaxies may be affected by merging events during their lifetime. Galaxy interactions are thought to flatten metallicity gradients as a consequence of chemical mixing as well as metal-poor gas inflows reaching the centre. This behaviour has indeed been observed e.g. in LIRGs at various merger stages (Rich et al. 2012), as well as optically and IR-selected early stage spiral–spiral interactions (Rupke, Kewley & Chien 2010). On the other hand, in a sample of 36 post-merger MaNGA galaxies, the local metallicity has been found to be suppressed in the outskirts while not being significantly affected in the central regions (Thorp et al. 2019).

While we have already attempted to exclude ongoing mergers from our analysis by identifying them visually from the SDSS multiband images as noted in Section 3, it is still possible for our sample to include post-merger galaxies that are no longer identifiable via morphological signatures. Therefore, while a full kinematic axis analysis is beyond the scope of this work, we perform a simple visual inspection of the stellar and gas-phase velocity maps taken from the MaNGA DAP with hybrid binning (Belfiore et al. 2019)[5] to identify galaxies that show potential signs of a misalignment between their stellar and gas-phase dynamics manifesting in different kinematic major axes of rotation. We point out that even this simple exercise can become challenging in the below-MS regime due to the weakness of the lines required to derive velocity maps. In general, we conclude that for the majority of our sample, the kinematics of the stellar and gas-phase components are consistent with rotating in an aligned manner. However, we flag a number of objects that show *potential* signs of misalignment. In detail, we verified that our results are not strongly affected when removing the AGN-like galaxies with the following IDs: 8588-6101, 8595-3703, and 8084-6103. Updated versions of Figs 2 and 8 excluding the targets listed above are presented in the appendix (Fig. F1).

Finally, it is still an open question for how long the optical and kinematic signature of mergers remain detectable. For instance, using `GADGET-3/SUNRISE` major merger simulations to construct mock velocity and velocity dispersion fields at the resolution of MaNGA, Nevin et al. (2021) broadly retrieve kinematic observability time-scales of 0.9–6 Gyr. On the other hand, Lotz et al. (2008) find that post-merger galaxies may become undetectable after just 200 Myr depending on merger parameters. We cannot exclude that long-term effects from past mergers affect our sample, but one may argue that any such effects on the gas-phase metallicities would be 'washed out' again by the other factors of influence that impact the chemical reservoir more imminently: *in situ* chemical evolution, inflows, and outflows. As mentioned in Section 4.1, while studies constraining the time-scale for metal redistribution are yet sparse, Simons et al. (2021) argue that it should be limited to $\lesssim$100 Myr, as otherwise galaxies may rapidly develop metallicity gradients more negative than observed (as predicted by modelling metal production based on observed SFR surface density profiles in $z \sim 1$ 3D-HST galaxies).

4.5 Morphological scenario

As mentioned already in Section 4.3, morphological effects may influence the gas properties and metal distribution within galaxies. For example, in a morphological quenching scenario (Martig et al. 2009), the gas disc would be stabilized against fragmentation and galaxies could thus retain a significant central gas reservoir diluting local metallicities e.g. from a recent inflow even at low star-forming activity. Using a compilation of different public optical-IFU data sets, Sánchez (2020) recently showed galaxies of different morphological types exhibited different shapes in their radial metallicity profiles (whilst also segregating into mass bins). In actively star-forming galaxies, Lutz et al. (2021) recently found evidence that the metallicity gradients are primarily set by variations in stellar mass surface density. From the resolved mass–metallicity relation (Rosales-Ortega et al. 2012; Sánchez et al. 2013; Barrera-Ballesteros et al. 2016), one may also expect metallicity gradients to be influenced by the stellar-mass surface density profiles in the low-$\Sigma_\star$ regime, although the scatter in the relation is large. We first use the stellar mass surface density within $1\,R_e$ ($\mu_\star = 0.5 \cdot M_\star/(\pi R_e^2)$) as a morphological tracer to assess broadly how morphological factors may contribute to our observed ∇Z–$t_{\rm dep}$ relation. In the left-hand panel of Fig. 12, we contrast the metallicity gradients to $\mu_\star$ for AGN, LINERs, and Composites, finding no correlation.

We then move to exploring the resolved profiles of stellar mass surface density as a function of ∇Z, using the results from our full spectral fitting procedure described in Section 2.3.3. In the right-hand panel of Fig. 12, we show our recovered profiles of stellar mass surface density $\Sigma_\star = M_{\star,\rm ann}/A_{\rm ann}$, denoting the mass of stars per surface area $A_{\rm ann}$ within a given annulus of width $0.2\,R_e$. The colour coding reflects a binning according to ∇Z (green/purple = objects with negative/positive metallicity gradients). The dotted lines denote the median profiles, and the spread is indicated by the shaded regions. Clearly, the two curves corresponding to different ∇Z bins are fully consistent with each other, such that we do not find any evidence for the stellar mass gradients being linked to metallicity gradients.

Finally, we also report that when using the Pipe3D v/σ ratio of velocity-over-velocity dispersion within $1.5\,R_e$ as a tracer of how rotation-dominated a given galaxy is, we find no trend with metallicity gradients, contrary to recent results at higher redshift (out to $z = 2.5$) by Sharda et al. (2021). Likewise, we report no correlation between ∇Z and the photometrically inferred bulge-to-total ratio B/T from the PyMorph catalog as a morphological tracer. Further, we find no relation with the central velocity dispersion within 2.5 arcsec of either the stellar kinematics $\sigma_\star$ (when excluding the single data point with lowest $\sigma_\star$) or the gas dynamics as traced by Hα. We thus conclude that, at least by using the simple morphological tracers in this section, we do not find any evidence for the metallicity gradients in our sample being influenced by morphological effects, contrary to the literature results summarized above. We note however that our sample size does not allow us to investigate the impact of morphology in separate mass bins. As a result, morphological trends may still be present, but could be diluted by the diversity of masses within our sample.

5 CONCLUSIONS

In this paper, we presented a selection of early results from the MASCOT survey (Wylezalek et al. 2022), focusing on an empirically

[5]In the hybrid binning scheme, the emission-line maps are providing line measurements in individual spaxels (while the stellar continuum is analysed in Voronoi bins).

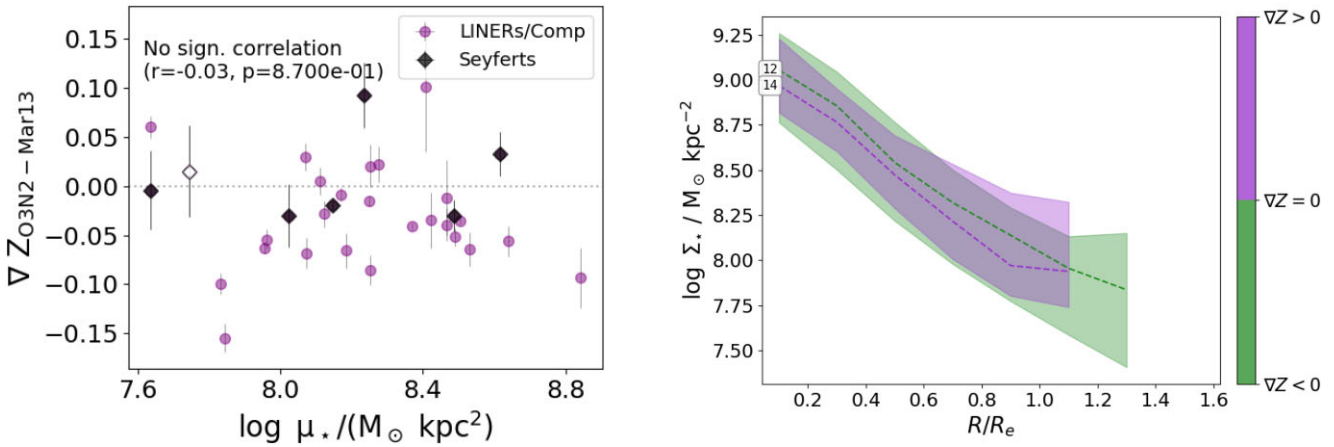

Figure 12. *Left-hand panel*: Metallicity gradients plotted against global stellar mass surface density $\mu_\star = 0.5 \times M_\star/(\pi {R_e}^2)$ as a tracer of morphology for AGN, LINERs, and Composites. We find no correlation. *Right-hand panel*: Median profiles of stellar mass surface density $\Sigma_\star$ as a function of galacto-centric radius in units of the half-light radius R_e. The colour-coding refers to bins of ∇Z where objects were divided into a bin with $\nabla Z > 0$ (purple) and one with $\nabla Z < 0$. The median profiles in each ∇Z bin are shown as dotted lines with associated spread illustrated by the shaded regions. Again, we find no link between ∇Z and stellar-mass surface density profiles.

found relation between gas-phase metallicity gradients ∇Z and molecular gas depletion times $t_{\rm dep}$ in LINERs, Seyfert AGN, and Composites below/on the MS. We used oxygen abundance gradients derived via the Marino et al. (2013) O3N2 calibrator, and specifically decided to explore the below/on-MS regime affected by DIG emission given recent results by e.g. Kumari et al. (2019), supporting the robustness of the O3N2 metallicity calibrator in DIG/LI(N)ER-dominated regions (as discussed in more detail in Section 2.4). We still exercised caution by using the metallicity gradients from the Pipe3D catalog, which were derived based on regions within galaxies that are pre-dominantly ionized by star formation. We excluded edge-ons, type 1 AGN, and visually identified major mergers from the analysis. Our primary results can be summarized as follows:

(i) The ∇Z–$t_{\rm dep}$ relation we report is strongly significant for our sample of 'AGN-like objects' combining AGN, LINERs, and Composites ($p \sim 0.001$, $r = 0.56$). When excluding Seyfert AGN (e.g. due to concerns about the accuracy of the metallicity gradients), the relation still holds for LINERs + Composites with $p \sim 0.005$, $r = 0.54$ (Fig. 2), while no relation is found in inactive galaxies.
The relation is intriguing given that variations in depletion time (or inversely, star forming efficiency) have been suggested to be the driving factor that pushes galaxies into the passive branch once they experienced an initial central lack of molecular gas (Colombo et al. 2020). In that sense, the discovery of a ∇Z–$t_{\rm dep}$ relation *below the MS* may suggest that whichever mechanism drives quenching in AGN-like objects also flattens or inverts metallicity gradients in the process.

(ii) The relation neither cannot be traced back to a link between ∇Z and MS offset, nor a trend with global SFR (Fig. 3). Further, we cannot explain the relation via the presence of mass effects, as we report no trend between ∇Z and stellar mass (Fig. 4), and none with inclination (Fig. 5).

(iii) We also checked that the relation persists when using a constant CO-to-H_2 conversion factor instead of a metallicity-dependent one (Fig. 6), and when using metallicity gradients based on the Tremonti et al. (2004) R23 calibrator instead of the Marino et al. (2013) O3N2 prescription (Fig. 7).

We then explored different possible physical drivers of the ∇Z–$t_{\rm dep}$ relation in AGN/LINERs/Composites in Section 4:

(i) We contemplated the scenario of metal redistribution via chemically enriched outflows, i.e. assuming ∇Z is flatter in galaxies with long depletion times because they are simplistically at a later evolutionary stage where feedback already had more time to operate. In AGN/LINERs/Composites, we indeed found a strong link between ∇Z and the mean width ('W_{80}'') of the ionized [O III] λ5007 line within 1 R_e (Fig. 8), as well as between W_{80} and $t_{\rm dep}$. We interpret this trend as a strong indication of feedback-induced chemical mixing taking place as galaxies transition to the red cloud.
Interestingly, the observed velocity broadening is very modest at < 500 km s^{-1}. However, in a picture where galaxies quench due to the integrated effect of feedback over prolonged time, weak feedback below the MS may represent a 'final push' that permanently decreases star-forming efficiencies. For a detailed discussion, including results from simulations, we refer the reader to Section 4.1.

(ii) We then analysed the impact of local star formation (at fixed stellar mass). Potentially, metallicity gradients may be traced back to local variations in star formation due to a resolved fundamental metallicity relation, which in turn may impact the global depletion time $t_{\rm dep} = M_{\rm H_2}/{\rm SFR}$. Indeed our sample of AGN/LINERs/Composites shows a connection between positive ∇Z/longer depletion times and a relative suppression of SFR surface density in the outskirts (Fig. 10), unlike inactive galaxies. Next to the impact of feedback, *in situ* star formation may thus contribute to shaping the ∇Z–$t_{\rm dep}$ relation in our AGN-like objects.

(iii) Similarly to outflows, inflows may influence metallicity gradients (though our galaxies reside below the MS). However, we find no trend when contrasting metallicity gradients to H_2 mass, CO luminosity, or molecular gas fraction $f_{\rm H_2} = M_{\rm H_2}/M_\star$ (Fig. 11), and thus no direct indication of gas accretion affecting the metallicity distribution. However, we note that our unresolved single-dish CO observations do not allow us to exclude the possibility of localized inflows influencing our results.

(iv) We further considered morphological effects. For instance, galaxies could decrease in star-forming efficiency whilst preserving a gas reservoir that is dynamically stabilized against fragmentation (Martig et al. 2009).
However, we find no evidence for metallicity gradients depending on stellar mass surface density within 1 R_e (Fig. 12), and no difference between the stellar mass surface density profiles of AGN-like objects

with positive and negative ∇Z. Using different morphological tracers – the v/σ ratio of velocity-over-velocity dispersion within 1.5 R_e, a photometrically inferred bulge-to-total mass ratio, or central velocity dispersion within 2.5 arcsec (stellar or H α) – offered no further clues.

(v) Given that merger activity would naturally impact the metallicity distribution within galaxies, we briefly search for merger signatures within our sample by visually comparing the H α and [O III] gas-phase velocity maps to the stellar velocity maps. We confirmed that our results were not strongly affected when conservatively discarding any galaxies that showed potential signs of misalignment in stellar and gas-phase kinematics.

In conclusion, we propose that in our AGN-like targets, the observed ∇Z–$t_{\rm dep}$ relation arises partially as a consequence of chemical mixing due to centrally driven (stellar or AGN) outflows that increase in impact as time goes on and depletion times become longer, and is partially connected to fluctuations in local star formation. The latter is consistent with a resolved fundamental metallicity relation, which may arise from a lack of diluting gas leading to both lower SFRs and higher local metallicities in the outskirts of quenching AGN-like objects.

We finally note that, given the sample size of our below-MS objects, we have not considered the impact of environment on metallicity in this work (e.g. enriched accretion onto satellites, see Schaefer et al. 2019). We defer an investigation of environmental effects on the molecular gas properties and other galaxy parameters using our full sample (below- and above-MS) to a later paper.

ACKNOWLEDGEMENTS

The entire MASCOT team would like to warmly thank the staff at the Arizona Radio Observatory, in particular the operators of the 12m Telescope, Clayton, Kevin, Mike and Robert, for their continued support and help with the observations. We further thank A. Bluck, B. Easeman, T. Davis, R. Maiolino, J. Piotrowska, P. Schady, J. Trayford, and S. Wuyts for fruitful discussions. We thank the referee S. F. Sánchez for helpful and constructive comments.

DW and CB are supported through the Emmy Noether Programme of the German Research Foundation. MA acknowledges support from FONDECYT grant 1211951, CONICYT + PCI + INSTITUTO MAX PLANCK DE ASTRONOMIA MPG190030, CONICYT+PCI + REDES 190194, and ANID BASAL project FB210003. WB acknowledges support from the ERC Advanced Grant 695671, 'QUENCH' and from the Science and Technology Facilities Council (STFC).

This research made use of MARVIN, a core PYTHON package and web framework for MaNGA data, developed by Brian Cherinka, José Sánchez-Gallego, Brett Andrews, and Joel Brownstein (Cherinka et al. 2019).[6]

This project makes use of the MaNGA-Pipe3D data products. We thank the IA-UNAM MaNGA team for creating this catalogue, and the ConaCyt-180125 project for supporting them.

Funding for the Sloan Digital Sky Survey IV has been provided by the Alfred P. Sloan Foundation, the U.S. Department of Energy Office of Science, and the Participating Institutions. SDSS-IV acknowledges support and resources from the Center for High Performance Computing at the University of Utah. The SDSS website is www.sdss.org. SDSS-IV is managed by the Astrophysical Research Consortium for the Participating Institutions of the SDSS Collaboration, including the Brazilian Participation Group, the Carnegie Institution for Science, Carnegie Mellon University, Center for Astrophysics | Harvard & Smithsonian, the Chilean Participation Group, the French Participation Group, Instituto de Astrofísica de Canarias, The Johns Hopkins University, Kavli Institute for the Physics and Mathematics of the Universe (IPMU) / University of Tokyo, the Korean Participation Group, Lawrence Berkeley National Laboratory, Leibniz Institut für Astrophysik Potsdam (AIP), Max-Planck-Institut für Astronomie (MPIA Heidelberg), Max-Planck-Institut für Astrophysik (MPA Garching), Max-Planck-Institut für Extraterrestrische Physik (MPE), National Astronomical Observatories of China, New Mexico State University, New York University, University of Notre Dame, Observatário Nacional / MCTI, The Ohio State University, Pennsylvania State University, Shanghai Astronomical Observatory, United Kingdom Participation Group, Universidad Nacional Autónoma de México, University of Arizona,University of Colorado Boulder, University of Oxford, University of Portsmouth, University of Utah, University of Virginia, University of Washington, University of Wisconsin, Vanderbilt University, and Yale University.

[6]http://sdss-marvin.readthedocs.io/en/stable/

DATA AVAILABILITY

The data underlying this article are available in Wylezalek et al. (2022) and its supplementary material, as well as on the MASCOT website: https://wwwstaff.ari.uniheidelberg.de/dwylezalek/mascot.html

REFERENCES

Accurso G. et al., 2017, MNRAS, 470, 4750
Alvarez-Hurtado P., Barrera-Ballesteros J. K., Sánchez S. F., Colombo D., López-Sánchez A. R., Aquino-Ortíz E., 2022, ApJ, 929, 47
Avery C. R. et al., 2021, MNRAS, 503, 5134
Baker W. M. et al., 2022, MNRAS, preprint (arXiv:2210.03755)
Baker W. M., Maiolino R., Bluck A. F. L., Lin L., Ellison S. L., Belfiore F., Pan H.-A., Thorp M., 2022b, MNRAS, 510, 3622
Baldwin J. A., Phillips M. M., Terlevich R., 1981, PASP, 93, 5
Barrera-Ballesteros J. K. et al., 2016, MNRAS, 463, 2513
Belfiore F. et al., 2017, MNRAS, 469, 151
Belfiore F. et al., 2019, AJ, 158, 160
Bertemes C., Wuyts S., 2022, MNRAS, submitted
Binette L., Magris C. G., Stasińska G., Bruzual A. G., 1994, A&A, 292, 13
Blanton M. R. et al., 2017, ApJ, 154, 28
Blanton M. R., Kazin E., Muna D., Weaver B. A., Price-Whelan A., 2011, ApJ, 142, 31
Bluck A. F. L. et al., 2020, MNRAS, 499, 230
Boardman N. et al., 2022, MNRAS, 514, 2298
Boardman N. F., Zasowski G., Newman J. A., Sanchez S. F., Schaefer A., Lian J., Bizyaev D., Drory N., 2021, MNRAS, 501, 948
Bolatto A. D. et al., 2017, ApJ, 846, 159
Brennan R., Choi E., Somerville R. S., Hirschmann M., Naab T., Ostriker J. P., 2018, ApJ, 860, 14
Brinchmann J., Charlot S., White S., Tremonti C., Kauffmann G., Heckman T., Brinkmann J., 2004, MNRAS, 351, 1151
Bruzual G., Charlot S., 2003, MNRAS, 344, 1000
Bundy K. et al., 2015, ApJ, 798, 7
Calzetti D., Armus L., Bohlin R. C., Kinney A. L., Koornneef J., Storchi-Bergmann T., 2000, ApJ, 533, 682
Carnall A. C. et al., 2019, MNRAS, 490, 417
Carnall A. C., McLure R. J., Dunlop J. S., Davé R., 2018, MNRAS, 480, 4379
Cazzoli S. et al., 2018, MNRAS, 480, 1106
Chauke P. et al., 2019, ApJ, 877, 48
Cherinka B. et al., 2019, AJ, 158, 74
Chisholm J., Tremonti C., Leitherer C., 2018, MNRAS, 481, 1690

Colombo D. et al., 2020, A&A, 644, A97
Comerford J. M. et al., 2020, ApJ, 901, 159
Concas A., Popesso P., 2019, MNRAS, 486, L91
Domínguez Sánchez H., Margalef B., Bernardi M., Huertas-Company M., 2022, MNRAS, 509, 4024
Ellison S. L., Patton D. R., Simard L., McConnachie A. W., 2008, ApJ, 672, L107
Ellison S. L., Thorp M. D., Pan H.-A., Lin L., Scudder J. M., Bluck A. F. L., Sánchez S. F., Sargent M., 2020, MNRAS, 492, 6027
Falcón-Barroso J., Sánchez-Blázquez P., Vazdekis A., Ricciardelli E., Cardiel N., Cenarro A. J., Gorgas J., Peletier R. F., 2011, A&A, 532, A95
Ferland G. J., Korista K. T., Verner D. A., Ferguson J. W., Kingdon J. B., Verner E. M., 1998, PASP, 110, 761
Fischer J. L., Domínguez Sánchez H., Bernardi M., 2019, MNRAS, 483, 2057
Franchetto A. et al., 2021, ApJ, 923, 28
Gibson B. K., Pilkington K., Brook C. B., Stinson G. S., Bailin J., 2013, A&A, 554, A47
Hemler Z. S. et al., 2021, MNRAS, 506, 3024
Hermosa Mu∼noz L., Márquez I., Cazzoli S., Masegosa J., Agís-González B., 2022, A&A, 660, A133
Janowiecki S., Catinella B., Cortese L., Saintonge A., Wang J., 2020, MNRAS, 493, 1982
Kauffmann G. et al., 2003, MNRAS, 346, 1055
Kennicutt R. C., 1998, ApJ, 498, 541
Kennicutt R. C., Evans N. J., 2012, ARA&A, 50, 531
Kewley L. J., Dopita M. A., Sutherland R. S., Heisler C. A., Trevena J., 2001, ApJ, 556, 121
Kewley L. J., Nicholls D. C., Sutherland R. S., 2019, ARA&A, 57, 511
Kroupa P., Boily C. M., 2002, MNRAS, 336, 1188
Kumari N., Maiolino R., Belfiore F., Curti M., 2019, MNRAS, 485, 367
Lacerda E. A. D. et al., 2018, MNRAS, 474, 3727
Lacerda E. A. D., Sánchez S. F., Mejía-Narváez A., Camps-Fari∼na A., Espinosa-Ponce C., Barrera-Ballesteros J. K., Ibarra-Medel H., Lugo-Aranda A. Z., 2022, New Astron., 97, 101895
Law D. R. et al., 2015, ApJ, 150, 19
Leja J., Carnall A. C., Johnson B. D., Conroy C., Speagle J. S., 2019, ApJ, 876, 3
Lian J. et al., 2018b, MNRAS, 476, 3883
Lian J., Thomas D., Maraston C., Goddard D., Comparat J., Gonzalez-Perez V., Ventura P., 2018a, MNRAS, 474, 1143
Lin L. et al., 2019, ApJ, 884, L33
Lin L. et al., 2020, ApJ, 903, 145
Lin L. et al., 2022, ApJ, 926, 175
López-Cobá C. et al., 2020, AJ, 159, 167
López-Cobá C., Sánchez S. F., Bland-Hawthorn J., Moiseev A. V., Cruz-González I., García-Benito R., Barrera-Ballesteros J. K., Galbany L., 2019, MNRAS, 482, 4032
Lotz J. M., Jonsson P., Cox T. J., Primack J. R., 2008, MNRAS, 391, 1137
Lutz K. A. et al., 2021, A&A, 649, A39
Ma X., Hopkins P. F., Feldmann R., Torrey P., Faucher-Giguère C.-A., Kereš D., 2017, MNRAS, 466, 4780
Maiolino R. et al., 2008, A&A, 488, 463
Maiolino R., Mannucci F., 2019, A&AR, 27, 3
Mannucci F., Cresci G., Maiolino R., Marconi A., Gnerucci A., 2010, MNRAS, 408, 2115
Marino R. A. et al., 2013, A&A, 559, A114
Martig M., Bournaud F., Teyssier R., Dekel A., 2009, ApJ, 707, 250
Martins L. P., González Delgado R. M., Leitherer C., Cervi∼no M., Hauschildt P., 2005, MNRAS, 358, 49
Mast D. et al., 2014, A&A, 561, A129
Nevin R. et al., 2021, ApJ, 912, 45
Noeske K. et al., 2007, ApJ, 660, L43
Oliveira C. B. Jr, Krabbe A. C., Hernandez-Jimenez J. A., Dors O. L. Jr, Zinchenko I. A., Hägele G. F., Cardaci M. V., Monteiro A. F., 2022, MNRAS, 515, 6093
Pettini M., Pagel B., 2004, MNRAS, 348, L59
Piotrowska J. M., Bluck A. F. L., Maiolino R., Peng Y., 2022, MNRAS, 512, 1052
Poetrodjojo H. et al., 2018, MNRAS, 479, 5235
Renzini A., Peng Y.-J., 2015, ApJ, 801, L29
Rich J. A., Torrey P., Kewley L. J., Dopita M. A., Rupke D. S. N., 2012, ApJ, 753, 5
Rosales-Ortega F. F., Sánchez S. F., Iglesias-Páramo J., Díaz A. I., Vílchez J. M., Bland-Hawthorn J., Husemann B., Mast D., 2012, ApJ, 756, L31
Rupke D. S. N., Kewley L. J., Chien L. H., 2010, ApJ, 723, 1255
Saintonge A. et al., 2017, ApJ, 233, 22
Saintonge A., Catinella B., 2022, ARAA, 60, 319
Salim S., 2014, Serb. Astron. J., 1, 1
Sánchez Almeida J., Sánchez-Menguiano L., 2019, ApJ, 878, L6
Sánchez S. F. et al., 2013, A&A, 554, A58
Sánchez S. F. et al., 2014, A&A, 563, A49
Sánchez S. F. et al., 2016, Rev. Mex. Astron. Astrofis., 52, 171
Sánchez S. F. et al., 2017, MNRAS, 469, 2121
Sánchez S. F. et al., 2018, Rev. Mex. Astron. Astrofis., 54, 217
Sánchez S. F. et al., 2021b, MNRAS, 503, 1615
Sánchez S. F., 2020, ARA&A, 58, 99
Sánchez S. F., Walcher C. J., Lopez-Cobá C., Barrera-Ballesteros J. K., Mejía-Narváez A., Espinosa-Ponce C., Camps-Fari∼na A., 2021a, Rev. Mex. Astron. Astrofis., 57, 3
Sánchez-Blázquez P. et al., 2006, MNRAS, 371, 703
Schaefer A. L. et al., 2019, ApJ, 884, 156
Schawinski K., Koss M., Berney S., Sartori L. F., 2015, MNRAS, 451, 2517
Schmidt M., 1959, ApJ, 129, 243
Sharda P., Wisnioski E., Krumholz M. R., Federrath C., 2021, MNRAS, 506, 1295
Simons R. C. et al., 2021, ApJ, 923, 203
Singh R. et al., 2013, A&A, 558, A43
Smee S. A. et al., 2013, ApJ, 146, 32
Stinson G. S., Bailin J., Couchman H., Wadsley J., Shen S., Nickerson S., Brook C., Quinn T., 2010, MNRAS, 408, 812
Thorp M. D., Ellison S. L., Simard L., Sánchez S. F., Antonio B., 2019, MNRAS, 482, L55
Trayford J. W., Schaye J., 2019, MNRAS, 485, 5715
Tremonti C. A. et al., 2004, ApJ, 613, 898
Tumlinson J., Peeples M. S., Werk J. K., 2017, ARA&A, 55, 389
Vale Asari N., Couto G. S., Cid Fernandes R., Stasińska G., de Amorim A. L., Ruschel-Dutra D., Werle A., Florido T. Z., 2019, MNRAS, 489, 4721
Vazdekis A., Sánchez-Blázquez P., Falcón-Barroso J., Cenarro A. J., Beasley M. A., Cardiel N., Gorgas J., Peletier R. F., 2010, MNRAS, 404, 1639
Wake D. A. et al., 2017, ApJ, 154, 86
Wylezalek D. et al., 2022, MNRAS, 510, 3119
Wylezalek D., Flores A. M., Zakamska N. L., Greene J. E., Riffel R. A., 2020, MNRAS, 492, 4680
Yan R. et al., 2016a, ApJ, 151, 8
Yan R. et al., 2016b, ApJ, 152, 197
Zhang K. et al., 2017, MNRAS, 466, 3217
Zheng Z. et al., 2017, MNRAS, 465, 4572

APPENDIX A: GALAXIES ABOVE THE MS DO NOT SHOW A ∇Z–$t_{\rm DEP}$ RELATION

In the work presented in this paper, we focused on galaxies located below the MS. For the purpose of a quick comparison, in Fig. A1, we check whether the MASCOT targets lying above the MS also show any correlation between their metallicity gradients ∇Z and their depletion time $t_{\rm dep}$, such as the ∇Z–$t_{\rm dep}$ relation seen in AGN-like objects below the MS (Fig. 2). In active and inactive galaxies alike (left-hand and right-hand panel, respectively), we do not find any correlation in the above-MS regime. For AGN-like objects, we further note that with the exception of the single data point with longest $t_{\rm dep}$ all metallicity gradients are negative in the above-MS systems in Fig. A1, while below the MS there are several (nine) AGN-like

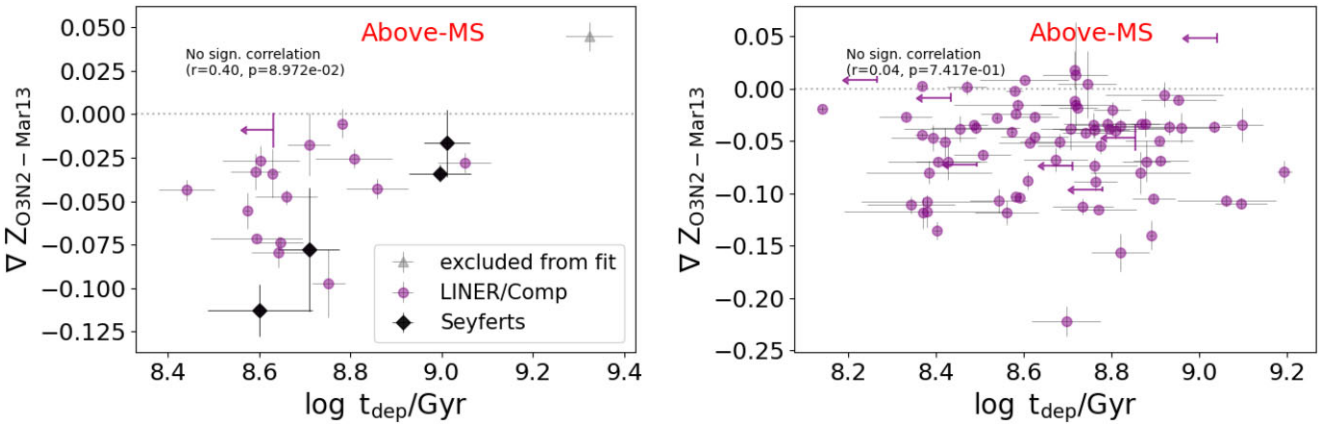

Figure A1. Location of *above-MS galaxies* from the MASCOT sample in the plane of metallicity gradients ∇Z against depletion time $t_{\rm dep} = M_{\rm H_2}/{\rm SFR}$. In the left-hand panel focusing on AGN/LINERs/Composites, Seyferts are highlighted in black, and the data points in grey is excluded to avoid it being the sole driver of our correlation analysis. The right-hand panel corresponds to inactive galaxies. The arrows denote upper limits for CO-undetected sources. Above the MS, there is no correlation in either case. Thus, the ∇Z–$t_{\rm dep}$ relation shown in Fig. 2 is unique to AGN-like objects located below the MS.

objects with positive gradients in Fig. 2. One complicating factor for systems above the MS is the higher contribution from stellar feedback that may not be limited to the central regions within galaxies and may affect both the metallicity distribution and the depletion time.

APPENDIX B: STATISTICAL BOOTSTRAPPING ANALYSIS

In this section, we use a bootstrapping approach to further test the statistical robustness of several key relations we presented herein. For each correlation, we use the associated sample to draw 1000 bootstrapped samples with replacement – these have the same number of data points as the original sample, but may feature repeated entries while omitting other points. For each such bootstrapped sample, we calculate an associated Spearman's rank coefficient to assess how the correlation changes when random data points drop out or are repeated. From the recovered distribution of r-values, we then proceed to calculate the 95 per cent confidence interval.

The results from this exercise are summarized in Table B1. The first two columns name the parameters that are subject of our correlation analysis in AGN-like objects. Specifically, we focus on the relations between metallicity gradients ∇Z, depletion time $t_{\rm dep}$, and mean [O III] W_{80} within 1 R_e (Figs 2 and 8). The median and 95 per cent confidence interval from our recovered distribution of r-values are listed in the third and fourth columns, while the fifth column specifies whether the statistical soundness of the correlation is confirmed (which holds if the 95 per cent confidence interval is not covering $r = 0$). The last column links to the figure illustrating each correlation.

The bootstrapping analysis suggests that all three correlations investigated in Table B1 are sound. ∇Z and $t_{\rm dep}$ are clearly correlated, with $r \in [0.25/0.76]$ and $<r> = 0.55$. Similarly, the correlations between resolved [O III] $W_{80}(< 1\,R_e)$ and ∇Z or $t_{\rm dep}$ are robust with $<r> = 0.7/0.82$ and $r \in [0.05/0.98]/[0.48, 0.97]$, respectively.

APPENDIX C: DISCUSSION ON THE INTERPRETATION OF THE [O III] LINE WIDTH AS A TRACER OF OUTFLOWS

In Section 4.1, we explored how the gas-phase metallicity gradients in our samples of AGN-like objects were impacted by outflows, using as a tracer the [O III] W_{80}, defined as the linewidth encompassing 80 per cent of the [O III] line flux. However, as discussed in Section 4.1, outflows are not the only drivers of emission-line broadening, such that W_{80} is not expected to be a pure tracer of outflows. While the W_{80} values are derived in single spaxels (e.g. without any stacking), individual spaxels still probe a finite range of radii and associated velocities that broadens emission lines, especially in central spaxels (while at large radii the rotation curve is flattening). Beam smearing could exacerbate this issue. The line broadenings we observe below the MS are weak, with W_{80} values staying below ~ 500 km s^{-1}, and could thus in principle be contaminated substantially potential well effects. We also note that there could be a complicating hidden dependency, since galaxies with a larger potential well may also harbour a more massive black hole, which may therefore drive stronger outflows, as well as increase W_{80}. In this section, we nevertheless conduct a number of sanity checks to reinforce our confidence in the use of the [O III] W_{80} parameter as a tracer of outflows.

In the left-hand and middle panels of Fig. C1, we first contrast the [O III] W_{80} values of the AGN-like objects against the stellar mass and stellar-mass surface density within one half-light radius $\mu_\star = 0.5 * M_\star/(\pi * R_e^2)$ as a direct tracer of the potential well. Seyfert AGNs

Table B1. Median r-values (Spearman's rank coefficient) and associated confidence intervals derived by a bootstrapping analysis for several of the correlations discussed in this work using 1000 bootstrapped samples.

Parameter A	Parameter B	Median r-value between A and B	95 per cent confidence interval on r	Confirming $r \neq 0$?	Figure
∇Z	$t_{\rm dep}$	0.55	[0.25, 0.76]	✓	Fig. 2
∇Z	[O III] $W_{80}(< 1R_e)$	0.7	[0.05, 0.98]	✓	Fig. 8
[O III] $W_{80}(< 1R_e)$	$t_{\rm dep}$	0.82	[0.48, 0.97]	✓	Fig. 8

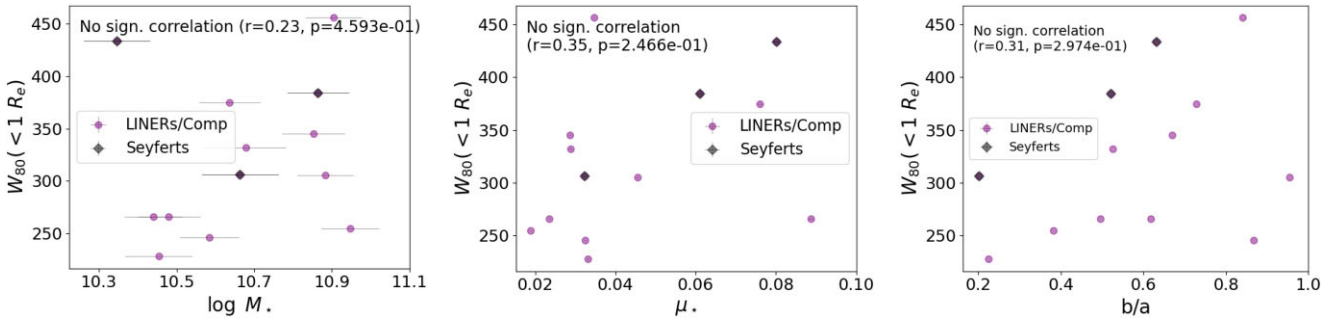

Figure C1. *Left-hand panel:* W_{80} values contrasted against stellar mass, yielding no significant correlation. *Middle panel:* W_{80} values plotted against stellar-mass surface density $\mu_\star = 0.5 * M_\star/(\pi * R_e^2)$, again showing no evidence for a correlation. *Right-hand panel*: W_{80} values contrasted against the minor-to-major axis ratio *b*/*a*. There is no correlation and specifically no evidence for artificially heightened W_{80} values in edge-on systems, where single spaxels may probe a larger diversity of radii.

are highlighted in black. In either case, there is no correlation. In the right-hand panel, we proceed to plot W_{80} against the minor-to-major axis ratio *b*/*a* tracing the inclination. If the W_{80} values were driven primarily by potential well effects, then edge-on systems would be most affected, since individual spaxels would probe a broader range of radii. However, we recover no evidence for ∇Z being inclination dependent.

APPENDIX D: USE OF OTHER MORPHOLOGICAL TRACERS

In this section, we return to the question of whether the metallicity gradients in our AGN-like objects are connected to their morphological states. While we found no obvious trends with stellar-mass surface density in Section 4.5, we here explore a variety of alternative morphological tracers.

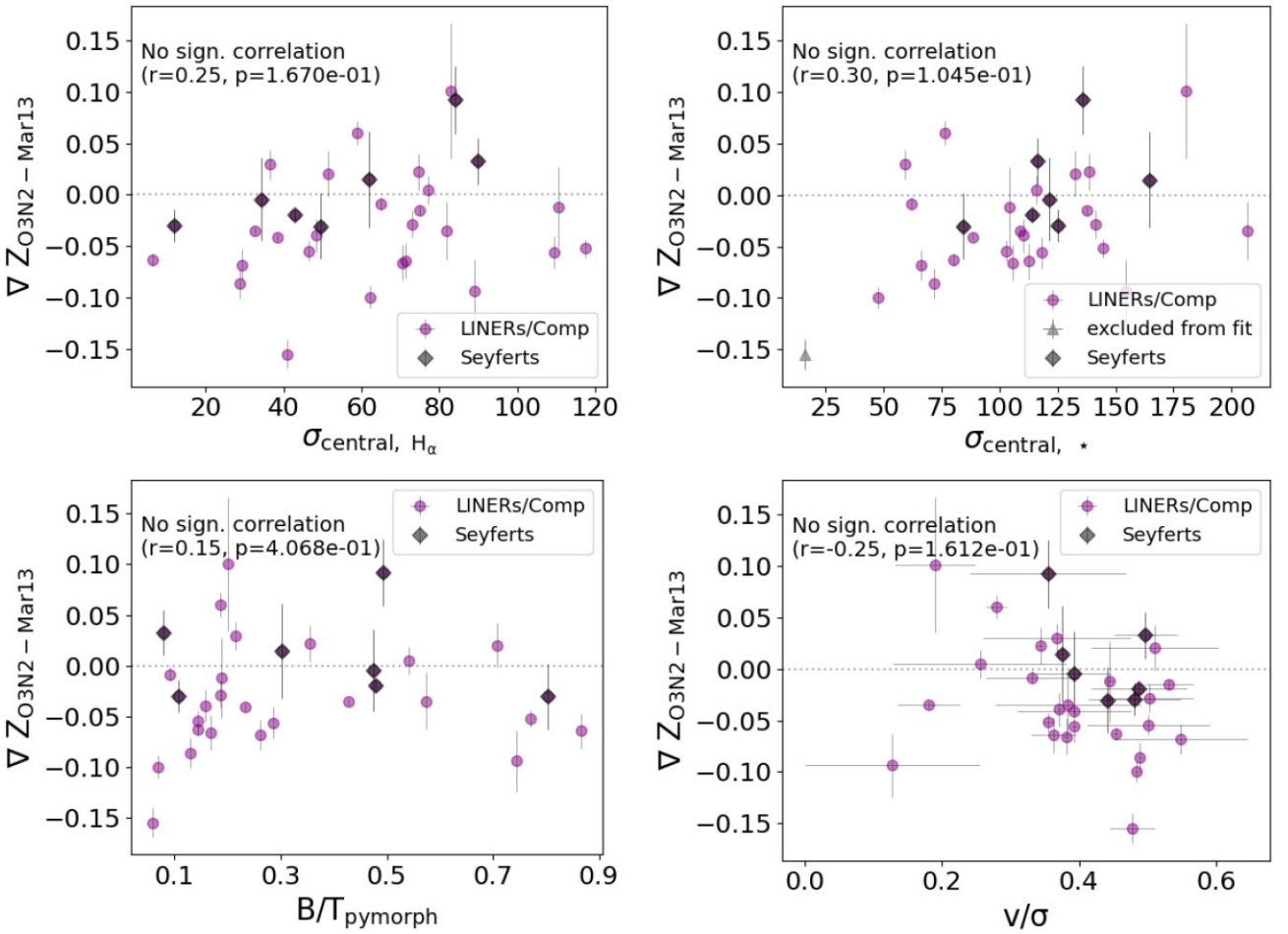

Figure D1. Metallicity gradients plotted against various morphological tracers: the velocity dispersion $\sigma_{\text{central, H}\alpha}$ (*top-left panel*), the central stellar velocity dispersion $\sigma_{\text{central},\star}$ (*top-right panel*), the bulge-to-total ratio *B*/*T* (*bottom-left panel*), and the *v*/σ ratio of velocity-over-velocity dispersion (*bottom-right panel*). We find no evidence for a correlation in either case.

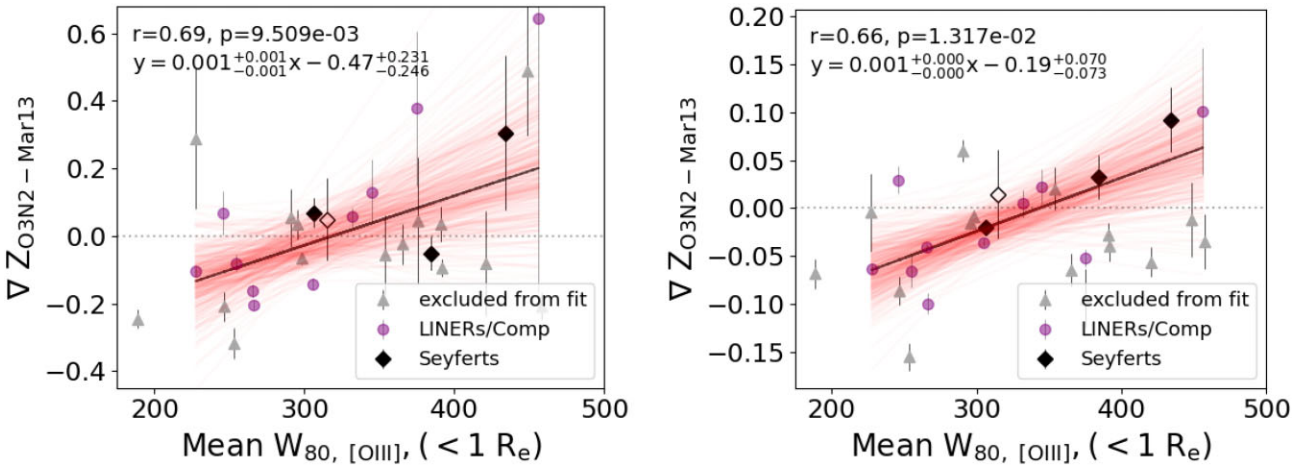

Figure E1. *Left-hand panel*: Same as Fig. 8, but based on the Tremonti et al. (2004) R23 metallicity diagnostic instead of the Marino et al. (2013) O3N2 prescription. *Right-hand panel*: Same as Fig. 8, but recalculating the depletion time with a constant CO-to-H_2 conversion factor $\alpha_{CO} = 4.36$ $M_\odot/(K\,km\,s^{-1}\,pc^{-2})$ corresponding to the canonical Milky Way value.

In Fig. D1, we contrast ∇Z to the central Hα velocity dispersion $\sigma_{\text{central, H}\alpha}$ (*top-left panel*), the central stellar velocity dispersion $\sigma_{\text{central},\star}$ (*top-right panel*), the photometrically inferred bulge-to-total ratio *B*/*T* (*bottom-left panel*), and the v/σ ratio of velocity-over-velocity dispersion (*bottom-right panel*) as a measure of how rotation-dominated a galaxy is and v/σ was taken from the Pipe3D catalog (Sánchez et al. 2016, 2018), while the *B*/*T* ratio was taken from the PyMorph catalog (Fischer, Domínguez Sánchez & Bernardi 2019; Domínguez Sánchez et al. 2022). In any case, we do not find any evidence for a link between morphology and metallicity gradients in AGN-like objects. This finding may be counter-intuitive, as one would expect the metallicity distribution to be affected by variations in local stellar-mass surface density according to the local mass–metallicity relation (Barrera-Ballesteros et al. 2016). Our results suggest that in AGN-like galaxies, the other drivers of metallicity gradients we identified – outflows and the distribution of star formation – play a more important role than the mass distribution.

APPENDIX E: THE ∇Z–W_{80} RELATION REVISITED WITH R23-BASED METALLICITIES OR CONSTANT α_{CO}

We now briefly explore how the $\nabla Z - W_{80}(< 1\,R_e)$ relation presented in Section 4.1 for AGN/LINERs/Composites below/on the MS may depend on our choice of metallicity calibrator or on assumptions about the metallicity dependence of the CO-to-H_2 conversion factor α_{CO}. In Section 3.2, we showed that the $\nabla Z - t_{dep}$ relation is still recovered when using the Tremonti et al. (2004) R23 diagnostic instead of the O3N2 calibrator, and also when using a constant CO-to-H_2 conversion factor based on the canonical Milky Way value rather than the metallicity-dependent conversion based on Accurso et al. (2017) used throughout the rest of the paper. We repeat this exercise for the $\nabla Z - W_{80}(< 1\,R_e)$ relation in Fig. E1, showing that the relation persists both when switching to the R23 metallicity calibrator (left-hand panel) or when setting $\alpha_{CO} \equiv 4.36$ $M_\odot/(K\,km\,s^{-1}\,pc^{-2})$ in the calculation of the depletion time (right-hand panel).

APPENDIX F: DISCARDING POTENTIAL POST-MERGER SYSTEMS

In this section, we briefly check that our results on AGN-like galaxies do not strongly depend on the inclusion of systems with potential post-merger signatures. As discussed in Section 4.4, we visually inspected the [O III] λ5007 and stellar velocity maps to search for kinematic misalignments between the stellar and gas-phase components as a potential sign of post-merger status. The maps were produced with `Marvin` (Cherinka et al. 2019) using hybrid binning with an *S*/*N* cutoff of 3. Fig. F1 shows the ∇Z–t_{dep} relation that we obtain when excluding the galaxies with the following Plate-IFUs: 8588-6101, 8595-3703, and 8084-6103. The relation remains robust. In Fig. F2, we further show that the relation between ∇Z and the [O III] line width within $1\,R_e$ remains significant when excluding those objects.

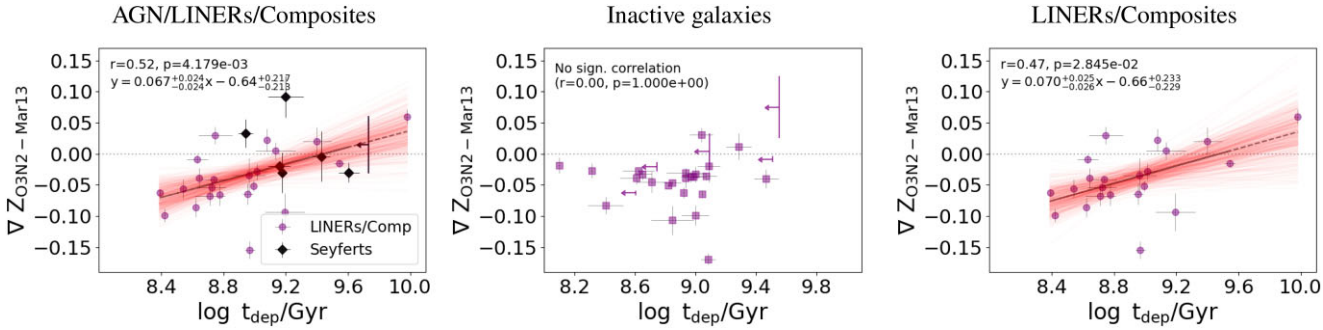

Figure F1. Same as Fig. 2, but excluding objects which show potential evidence for a misalignment between their stellar and gas-phase kinematics.

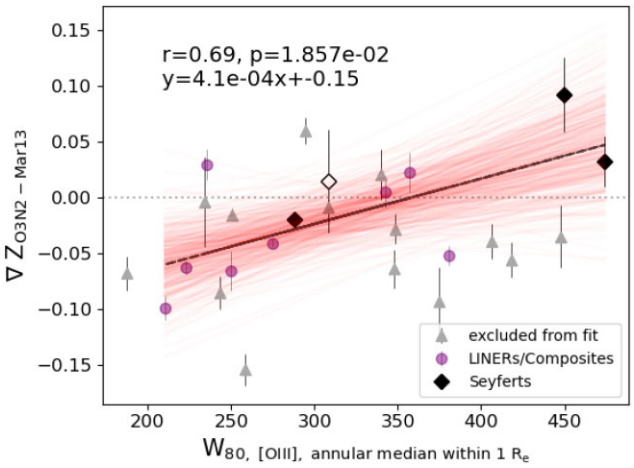

Figure F2. Same as Fig. 8, but excluding objects which show potential evidence for a misalignment between their stellar and gas-phase kinematics.

This paper has been typeset from a TEX/LATEX file prepared by the author.